Salient features of wheel-vehicle aerodynamic interactions: Consequences for drag

D. Bao, J. Borée, C. Sicot, C. Roebroeck

Salient features of wheel-vehicle aerodynamic interactions: consequences for drag

D. Bao[a]*, J. Borée[a], C. Sicot[a], and C. Roebroeck[b]

[a] Institut Pprime, UPR-3346 CNRS – ISAE-ENSMA – Université de Poitiers, Futuroscope Chasseneuil, France.
[b] MFP Michelin, Site de LADOUX, Clermont-Ferrand, France.

Abstract

Salient features of wheel–vehicle interactions and their consequences for drag are investigated experimentally based on a simplified square-back vehicle with different distances l between the rear wheels and the base of the vehicle. Two different mechanisms responsible for a base drag increase of up to 12% are distinguished. At the scale of the vehicle, whatever the distance l, wheels perturb the underflow and induce a global variation of the vertical balance of the vehicle wake. According to the state of the initial wake, significant base drag increase or decrease are observed. Considering the scale of the wheels, if the wheel-to-base distance l/w (w being the width of the wheels) is smaller than a threshold of order 3 in the present configuration, the base drag increases and is very sensitive to l/w. In this situation, a mean mass transfer from the vehicle wake to the wake of the rear wheels is observed. Based on these observations, a physical model is then proposed to explain this high-sensitivity regime.

Keywords: automotive aerodynamics, wheels, wake.

1. Introduction

Drag reduction of ground vehicles has always been an important topic due to energy and environmental issues. At highway speeds with high energy consumption, the aerodynamic drag accounts for over 50 % of the total drag (Schuetz, 2016). The wheels and their interactions with the main body of the vehicle account for more than 25% of the aerodynamic drag (Wickern *et al.*, 1997). In particular, indirect effects of the wheels leading to an increase in the base drag will have a very detrimental effect on the total drag of the vehicle. The optimization of the wheel drag is often restricted by functionality issues. Therefore, understanding the salient features of wheel-vehicle interactions is of particular importance for drag reduction.

Several aspects of wheel-vehicle interactions were considered in previous studies. Adding fixed or rotating wheels to a vehicle results in an important drag increase (Wickern *et al.*, 1997; Regert & Lajos, 2007; Huminic & Huminic, 2017; Wang, 2019; Pavia, 2019). The flow field was studied and it was found that wheels lead to modifications at the scale of the vehicle, such as a reduction in the underflow momentum and a change in the vertical balance of the vehicle wake.

The effect of wheel rotation was specifically studied by actuating the wheels on a fixed ground or by using moving ground facilities (Cogotti, 1983; Mercker & Knape, 1989; Le Good *et al.*, 1998; Elofsson & Bannister, 2002; Heft *et al.*, 2012; Pavia & Passmore, 2017; Wang *et al.*, 2019, 2020; Rejniak & Gatto, 2021; Yu *et al.*, 2022; Aultman *et al.*, 2022). On a given set-up, comparing fixed and rotating wheel configurations, it was found that rotation is responsible for a moderate drag change (mostly drag decreases). Global changes at the scale of the vehicle were also measured for example in Elofsson & Bannister (2002) and Wang *et al.* (2020). Moreover, changes in the

*Corresponding author. Email address: di.bao@ensma.fr (D.Bao)

local interactions between the rear wheel wakes and the vehicle wake were proposed in Elofsson & Bannister (2002) and Wäschle (2007) as possible reasons for the changes in drag. However, the interaction mechanisms at the scale of the rear wheels were not revealed in these two studies.

A third aspect concerning geometrical modifications of the wheels was studied for drag reduction. Some geometrical modifications (for example, the shoulder profile (Wittmeier *et al.*, 2014), the rim design (Landström *et al.*, 2009, 2011; Brandt *et al.*, 2019; Josefsson *et al.*, 2022*b*), and the tire pattern (Hobeika *et al.*, 2013; Hobeika & Sebben, 2018; Reiss *et al.*, 2019; Josefsson *et al.*, 2022*a*)) were found able to reduce the wheel drag. However, these local changes also induce modifications of the wheel-vehicle interactions which may compensate for or even dominate the local gains, leading to an increase in total aerodynamic drag. This can be seen in Hobeika *et al.* (2013) by applying different wheel geometries on two types of cars: a sedan and a sports wagon. From a more industrial point-of-view, Wittmeier *et al.* (2013) installed different tires having the same dimensions on several road vehicles. They found that the ranking by the aerodynamic drag of different tires sometimes depends on vehicle geometry.

These previous studies, to some extent, revealed the two main aspects of the wheel-wake interactions. The first one is the global modifications in the underflow and in the equilibrium of the vehicle wake. The second one is the local interactions between the rear wheels and the vehicle wake. However, these two aspects, especially the second one, remain to be understood in detail. To this aim, Wang (2019) proposed that at first order, the wheels can be seen as underflow geometric perturbations. Model obstacles were then introduced in the underflow of a square-back vehicle and were found to have the same effects on the flow and on the drag as the wheels. Most importantly, the key aerodynamic features, the underflow blockage, the development of the wakes of the wheels and their interactions with the near-wake of the vehicle, are represented. Using this simplified method, a parametric study was performed in Bao *et al.* (2022) by perturbing the underflow of a simplified square-back vehicle using a pair of two-dimensional (2-D) D-shaped obstacles. By systematically varying the obstacle width and the relative distance from the obstacles to the base of the vehicle, the sensitivity of the base drag of the vehicle was revealed. Furthermore, a salient feature of the local near-wake interactions was found to be a mean mass transfer from the wake of the vehicle to the wakes of the obstacles. This feature was then linked to the base drag changes using a physical model.

In the present work, the wheel-vehicle interactions are investigated experimentally based on a simplified square-back vehicle with wheels. We focus on the base drag evolution and large-scale dynamics of the near wake because the base drag is the major drag contributor for this type of vehicle (Schuetz, 2016). Our choice is to follow the investigation in Bao *et al.* (2022), by selecting the distance between the rear wheels and the base of the vehicle as the main parameter. This is also based on the fact that a wide range of relative distances can be found for different car types in the market. Our goal is first to analyze how the wake and drag of the vehicle are globally modified by the presence of the wheels. The second goal is to reveal in detail what are the salient features of the local interactions between the rear wheels and the vehicle wake. The experimental apparatus used for this study are detailed in §2, followed by a description of the baseline flow without the wheels in §3. By installing the wheels and varying the wheel-to-base distance, the salient features of wheel-vehicle interactions are revealed in §4. The influence of large-scale asymmetry of the vehicle wake is then presented in §5. Concluding remarks are proposed in §6.

2. Experimental set-up

2.1. Wind tunnel facility and model geometry

The experiments are performed in the S620 closed-loop wind tunnel of ISAE-ENSMA having a 5 m-long test section with a 2.4×2.6 m^2 rectangular cross-section. Under most operating conditions, the turbulence intensity of the incoming flow is of the order of 0.3 % and the spatial inhomogeneity is lower than 0.5 %. The arrangement inside the test section and the coordinate system are schematically given in figure 1(a).

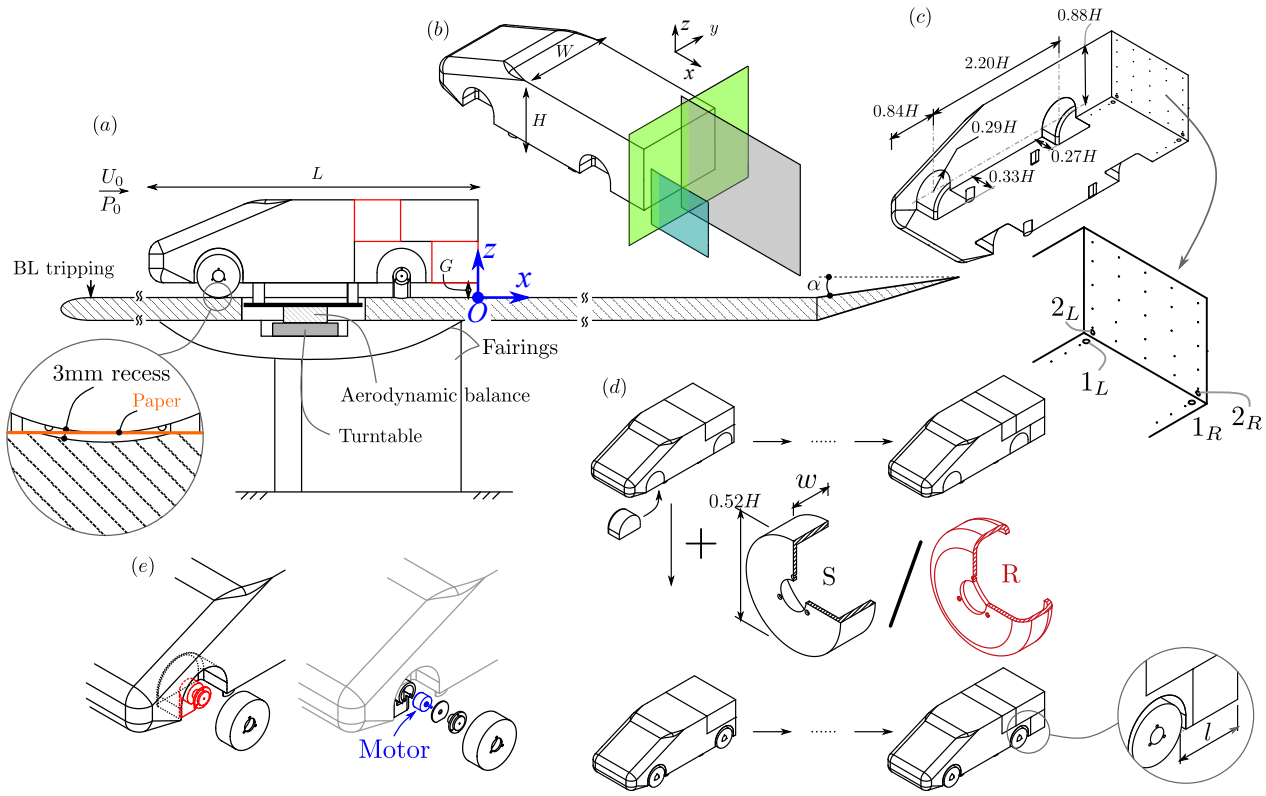

Figure 1: Experimental set-up. (a) Arrangement of the vehicle model and the raised floor in a subsonic wind tunnel. (b) Isometric view of the model and particle image velocimetry (PIV) fields of view (FOVs) in the symmetry plane of the vehicle ($y/H = 0$, colored in gray), symmetry plane of the left-hand side wheels ($y/H = -0.58$, colored in blue), and cross-flow plane ($x/H = 0.03$, colored in green). (c) Dimensions of the wheelhouses and the locations of pressure taps. Points indicate locations of mean pressure measurements and circles indicate locations of time-resolved pressure measurements. (d) Test groups consist of baseline cases and cases with either sharp-edged-shoulder wheels (S) or rounded-shoulder wheels (R). A detailed sketch of how the wheels are installed is given in (e).

A square-back simplified vehicle (isometric view in figure 1b), usually referred as the Windsor body (Pavia *et al.*, 2020; Varney *et al.*, 2020), is fixed in proximity to a raised floor by four profiled struts with a ground clearance $G = 0.05$ m (around five times the thickness of the incoming boundary layer). Four wheelhouses with dimensions and locations detailed in figure 1(c) are equipped on this vehicle. The width W and height H of the vehicle are 0.389 m and 0.289 m, respectively. Seven vehicle lengths $L/H = \{3.41, 3.49, 3.59, 3.68, 3.78, 3.87, 3.97\}$ are considered by changing the size of the plates colored in red in figure 1(a). At the front of the vehicle, all the leading edges are rounded with a radius of $R = 0.05$ m except the edge of the roof, which has a radius of 0.2 m. Before installing the vehicle on the floor, the streamwise pressure gradient above the floor is compensated by a flap located at the trailing edge of the floor, which is regulated to $\alpha = 2°$. The blockage ratio above the floor caused by the model is 2.4 %, which makes blockage correction unnecessary.

Two types of wheels are used for the present study and are shown in figure 1(d). These wheels are of the same diameter $0.52H$ and width $w = 0.19H$. They are machined from solid aluminum and have a hollow shape to reduce inertia. Different shoulder radii are considered for the two types of wheels. For the wheel type S, the shoulders are sharp edges. On the other hand, for the wheel type R, the shoulders are rounded with a radius of $0.3w$. This radius is chosen based on the average of several tire shoulder radii found in the market (e.g. 205/55R16, 235/55R19).

Inside each wheelhouse as shown in figure 1(e), an electrical motor (Maxon EC 45) is fixed on the floor through a profiled support and is therefore not in contact with the vehicle. The wheels are then installed on the motors. Before the experiments, the location of each wheel is carefully adjusted to make the wheel flush to the side of the vehicle, tangent to the floor, and with the axis in the symmetry plane of the corresponding wheelhouse. Similar to Pavia (2019) and Varney (2020),

a 3 mm deep recess is designed to prevent contact between the wheel and the floor as shown in the inserted figure of figure 1(a). However, preliminary tests with stationary wheels showed that the resulting gap flow has influence on the base pressure, maximally leading to $\sim 5\%$ base drag decrease. The gap is therefore sealed by placing a kraft paper between each wheel and the floor as shown in figure 1(a), producing negligible differences in pressure measurements compared to the situation when the recess is fully sealed by high-density foam. During the experiments, The wheels are always rotated at the speed of 3187 RPM matching the free-stream velocity. Additional comments and analyses on the effects of wheel state (rotating or stationary) are given in appendix A.

All the results presented are collected under a free-stream velocity $U_0 = 25$ m s^{-1}, corresponding to a height-based Reynolds number $Re_H = U_0 H/\nu = 4.8 \times 10^5$, where ν is the kinematic viscosity of the air at operating temperature. The same Windsor model equipped with sharp-edged-shoulder wheels was tested in Varney (2020). It was found that the model is Reynolds insensitive when the test is conducted above the Reynolds number selected for the present study. The origin O of the coordinate system (x, y, z) (shown in figure 1a behind the vehicle) is always located at the intersection point of the floor, the rear surface (the base) and the symmetry plane of the vehicle, with x, y and z defined, respectively, along the streamwise, spanwise and floor-normal directions. Under this system, the velocity vector is decomposed into $\boldsymbol{u} = (u_x, u_y, u_z)$. Unless otherwise stated, all physical quantities are normalized by any appropriate combination of the model height H, the free-stream velocity U_0 and the air density ρ during the measurements. The Reynolds decomposition is employed to decompose a quantity $\mathcal{X}$ into $\mathcal{X} = \overline{\mathcal{X}} + \mathcal{X}'$, where $\overline{\mathcal{X}}$ and $\mathcal{X}'$, respectively, denote its time-averaged and fluctuating components.

Several factors of the present set-up that may influence the results are now discussed. First of all, the floor is fixed and the ground boundary layer reduces the flow momentum under the vehicle compared to moving floor condition (Krajnović & Davidson, 2005; Strachan *et al.*, 2007). Two different vehicles with stationary wheels, namely a sedan and a square-back, were tested by Elofsson & Bannister (2002) to investigate the effect of moving floor. It was found to have a very slight effect on the aerodynamic drag. In the present situation where the ground boundary layer is taken care of by the raised floor, we expect a slight change in the wake equilibrium of the vehicle. An investigation of different wake asymmetries is conducted in section 5. In addition, the contact patches between the wheels and the floor are not considered due to the non-deformable shape of the model wheels. In Mlinaric & Sebben (2008), the influence of contact patch size on a passenger car was investigated. It was concluded that tire deflection has a limited effect on the drag of the car and that the flow field is only changed locally near the contact patches of the wheels. A similar observation was made in Yu *et al.* (2020). One important hypothesis of this research is that, at first order, the wheel wake development is responsible for the local near-wake interactions between the rear wheels and the main wake. The results presented in what follows support this hypothesis. While an accurate representation of the contact patch - very difficult at a reduced scale (Wäschle, 2007; Wittmeier *et al.*, 2014) - is needed to obtain quantitative results on a specific car configuration, the use of rigid wheels is justified to focus on the main physical contributions, which is the goal of the present work.

2.2. Test groups

L/H	3.41	3.49	3.59	3.68	3.78	3.87	3.97
Baseline group	×	×	×	×	×	×	×
Wheel group S	×	×	×	×	×	×	×
Wheel group R	×	-	-	-	-	-	×

Table 1: Cases considered for each test group.

The cases tested are categorized into different groups and are summarized in table 1. First, four plugs are used to fill the wheelhouses as shown in figure 1(d). The seven different lengths are tested

in this situation which forms the baseline group. For the wheel group S (sharp-edged shoulder), the seven different lengths are tested. On the other hand, for the wheel group R (rounded shoulder), only the shortest and the longest vehicle lengths are tested. The distance l from the rear wheels to the base (see figure 1d) is varied thanks to the variation in the vehicle length, which gives $l/w = \{0.65, 1.08, 1.58, 2.08, 2.58, 3.08, 3.58\}$. The l/w range considered here includes the l/w values for typical road square-back vehicles, from mini vehicles for example Smart Fortwo W453 ($l/w = 0.52$) to big Multi-Purpose Vehicles (MPVs) for example Mercedes-Benz V-class W447 ($l/w = 3.46$).

2.3. Pressure measurements

Two different pressure measurement systems are used to perform surface pressure measurements. The first one used for time-averaged and long-timescale measurements includes two 64-channel ESP-DTC pressure scanners linked to 1 mm diameter pressure taps located around the model by 78 cm long vinyl tubes. 25 taps on the base and 6 taps on the underside (see figure 1c) are used in the present work. The taps on the base and on the underside are connected, respectively, to the two scanners with ranges of ± 1 and ± 2.5 kPa. The accuracy of the two scanners lies respectively below ± 1.5 and ± 3.75 Pa. Acquisitions from the scanners are conducted at a sampling rate of 100 Hz.

The second system dedicated to time-resolved measurements contains four differential pressure sensors (SensorTechnics HCLA 02X5DB) connected to the pressure taps located on the base and the underside using 64 cm tubes. These taps are numbered as $n_{L,R}$ ($n \in [1, 2]$) as shown in figure 1(c), where L and R denote the left-hand and right-hand sides, respectively. The measurements are a posteriori calibrated and corrected to compensate for the pressure distortions induced by the tubings so that the frequency response of the system is flat on the whole frequency range considered in the present study. A sampling frequency of 2000 Hz is used for this system with an accuracy of ± 0.7 Pa.

The pressure coefficient C_p is used to express the pressure measurements and is defined as:

$$C_p = \frac{p - p_0}{0.5\rho U_0^2}, \tag{1}$$

where the reference static pressure p_0 is always obtained at $2.4H$ downstream the front of the vehicle from a Pitot tube installed at the ceiling of the test section. For all the cases gathered, the duration of the pressure measurements is 300 s. For the baseline case presenting lateral bimodal behavior on a long-timescale of the order of $O(10^3 H/U_0)$ (Grandemange *et al.*, 2013), this measurement duration is not sufficient to obtain complete statistical convergence. Nevertheless, this time window is chosen as a compromise between a reasonable duration of the experimental campaign and a satisfactory convergence of the mean base pressure. For a baseline case having a horizontal bi-stable wake, the standard deviation of mean base pressure values obtained from repeated measurements is found to be less than 1% of the average value.

Using the 25 pressure measurements on the base, a function of C_p is generated for the whole surface in order to calculate the pressure drag from the base:

$$C_B = \frac{-\int_B C_p ds}{HW}, \tag{2}$$

where B represents the base surface. The asymmetry of the vehicle wake is characterized by the position of the base center of pressure (CoP) (y_b, z_b) relative to the center of the base of coordinates $(0, 0, G + H/2)$. The two components of the CoP are calculated via:

$$y_b = \frac{\sum_{i=1}^{25} y_i C_p(y_i, z_i, t)}{\sum_{i=1}^{25} C_p(y_i, z_i, t)}, z_b = \frac{\sum_{i=1}^{25} (z_i - G - H/2) C_p(y_i, z_i, t)}{\sum_{i=1}^{25} C_p(y_i, z_i, t)}. \tag{3}$$

In the same fashion as Varney (2020), the mean horizontal component of the base CoP $\overline{y_b/H}$ is used to achieve the zero yaw condition based on a pressure measurement of 10 minutes (i.e. 5×10^4 convective time units H/U_0). The turntable as shown in figure 1(a) is used to yaw the baseline

Planes	set-up	x/H range	y/H range	z/H range	Vector spacing
vehicle symmetry plane	2D2C	[0, 2.7]	-	[0, 1.6]	0.0045H
wheel symmetry plane	2D2C	[0, 1.0]	-	[0,0.9]	0.0023H
Cross-flow plane	2D3C	-	[-1.4,1.4]	[0,1.3]	0.0034H

Table 2: Details of PIV fields of view.

vehicle with an increment of 0.1°. The mechanical yaw angle with the minimum $|\overline{y_b/H}|$ is found to be 0.1° and is chosen as the zero yaw condition.

For detailed investigations of pressure measurements, we define $\langle C_p \rangle$ as the spatial-averaged pressure coefficient from the left-hand L and right-hand R sides of the vehicle in order to reduce the influence of any residual asymmetry of the vehicle wake:

$$\langle C_p \rangle = \frac{1}{2}(C_p(y_i, z_i, t) + C_p(-y_i, z_i, t)). \tag{4}$$

For the spectral information obtained from the differential pressure sensors, the same space-averaging is also applied for the spectra.

2.4. Aerodynamic force measurements

A six-component aerodynamic balance (9129AA Kistler piezoelectric sensors and 5080A charge amplifier) connected to the model is used to quantify the aerodynamic drag acting on the model. Measurements are performed at a sample rate of 200 Hz with a total accuracy below 0.6 % of the full range, representing 1 % in the mean drag force $\overline{F_x}$. A low-pass filter at 10 Hz is applied directly to the charge amplifier to limit high-frequency noise. The drag coefficient is defined as:

$$C_D = \frac{F_x}{0.5\rho U_0^2 HW}. \tag{5}$$

The force measurements are always performed simultaneously with the pressure measurements with the same sampling duration. Therefore, the same conclusion regarding statistical convergence is achieved.

2.5. Velocity measurements

The velocity fields in the near wake are measured by a particle image velocimetry (PIV) system. The system consists of a Quantel EverGreen 2 × 200mJ laser and two LaVision Imager LX 16 Mpx cameras. The seeding of the flow is introduced downstream of the raised floor and recirculates through the tunnel closed circuit. Particles with diameter of 1 μm are generated by atomization of mineral oil. Three two-dimensional fields of view (FOVs) are considered as depicted in figure 1(d). The first one located in the cross-flow plane ($x/H = 0.03$) in proximity to the base of the vehicle is of stereoscopic (2-D three-component (2D3C)) set-up, capturing three velocity components. The other two FOVs respectively located in the symmetry planes of the vehicle ($y/H = 0$) and of the left-hand rear wheel ($y/H = -0.58$) are of 2-D two-component (2D2C) set-up, obtaining the streamwise u_x and vertical u_z velocity components. The details of the PIV FOVs are given in table 2.

For representative cases, 1200 pairs of images are captured from each FOV at a sample rate of 4 Hz, which is satisfactory for statistical convergence of first- and second-order statistics. The image pairs are processed using DaVis 10.1 with a final interrogation window of 16 × 16 pixels for all FOVs. All the processing is performed with an overlap of 50 %. The resulting vector spacing for each measurement plane is summarized in table 2. The maximum uncertainty on the instantaneous velocity fields from different FOVs considering an absolute displacement error of 0.1 pixels is estimated to be less than $0.01U_0$.

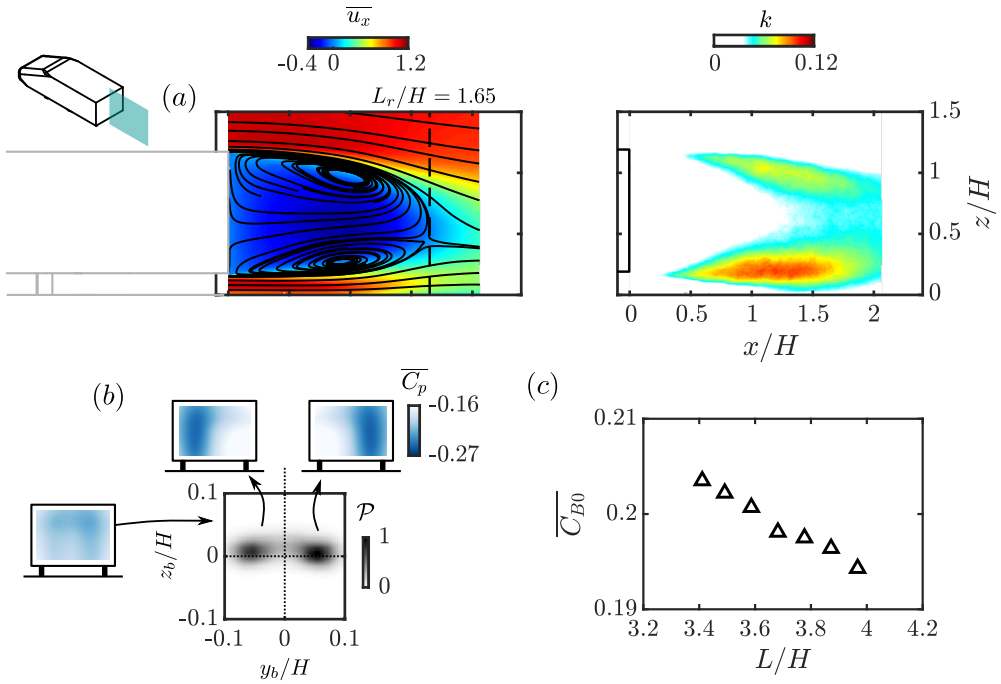

Figure 2: Baseline flow for the longest vehicle $L/H = 3.97$. (a) Mean streamwise velocity $\overline{u_x}$ and turbulent kinetic energy $k = (\overline{u'_x u'_x} + \overline{u'_z u'_z})/2$ in the symmetry plane of the vehicle $y/H = 0$. (b) Conditional averaging of the base pressure distribution based on the joint probability density function (p.d.f.) of the base CoP position. (c) Evolution of the base drag $\overline{C_{B0}}$ with the length of the vehicle L/H.

3. Baseline flow

Before installing the wheels on the vehicle model, we briefly characterize the baseline cases. To this end, the wake flow for the longest baseline vehicle $L/H = 3.97$ is presented in figure 2.

The mean streamlines in the symmetry plane of the vehicle ($y/H = 0$) describe a wake with vanishing vertical asymmetry. The length of the recirculation region is quantified by:

$$L_r = max(x)_{\overline{u_x} \leq 0}. \tag{6}$$

The global topology is qualitatively similar to the wake captured in Pavia *et al.* (2020) using also a Windsor body (their vehicle length is shorter). As detailed in Haffner *et al.* (2020), a weak interaction between the top and bottom shear layers is observed for this type of wake. Depicting the mean turbulent kinetic energy $k = (\overline{u'_x u'_x} + \overline{u'_z u'_z})/2$, almost balanced turbulent levels are noticed between the top and bottom shear layers. Therefore, with the underflow perturbed later by the wheels, a change in the vertical wake balance may lead to a drag increase as shown in Bao *et al.* (2022), Perry & Passmore (2013) and Haffner *et al.* (2021).

In the horizontal direction, the wake exhibits the well-known long-time random switching motion (Grandemange *et al.*, 2013) with two equiprobable states as presented in figure 2(b). The two states are given by the joint probability density function (p.d.f.) of the two components of the base CoP position. Further conditional averaging based on the sign of the horizontal component of the base CoP position y_b/H provides the base pressure distributions of the two wake states shown in figure 2(b), which represent wake topologies dominated by a large recirculating flow at the left-hand and right-hand sides, respectively.

The evolution of base drag and total drag coefficients with the length of the vehicle is displayed in table 3. From the case $L/H = 3.97$ described before, there is a continuous increase of base drag with reducing L/H (also plotted in figure 2c), while the total drag is approximately constant. The difference between the two variations can be attributed to the reduction in the friction drag with decreasing model length. The measurements show that the wake characteristics shown in figure 2(a) remain the same for all the lengths (only the recirculation length L_r is shown in table 3 for brevity).

L/H	3.41	3.49	3.59	3.68	3.78	3.87	3.97
$\overline{C_{B0}}$	0.204	0.202	0.201	0.198	0.198	0.196	0.194
$\overline{C_{D0}}$	0.225	0.226	0.226	0.226	0.226	0.225	0.225
L_r/H	1.66	1.66	1.66	1.66	1.65	1.64	1.65

Table 3: Evolution of the mean aerodynamic characteristics with the model length L.

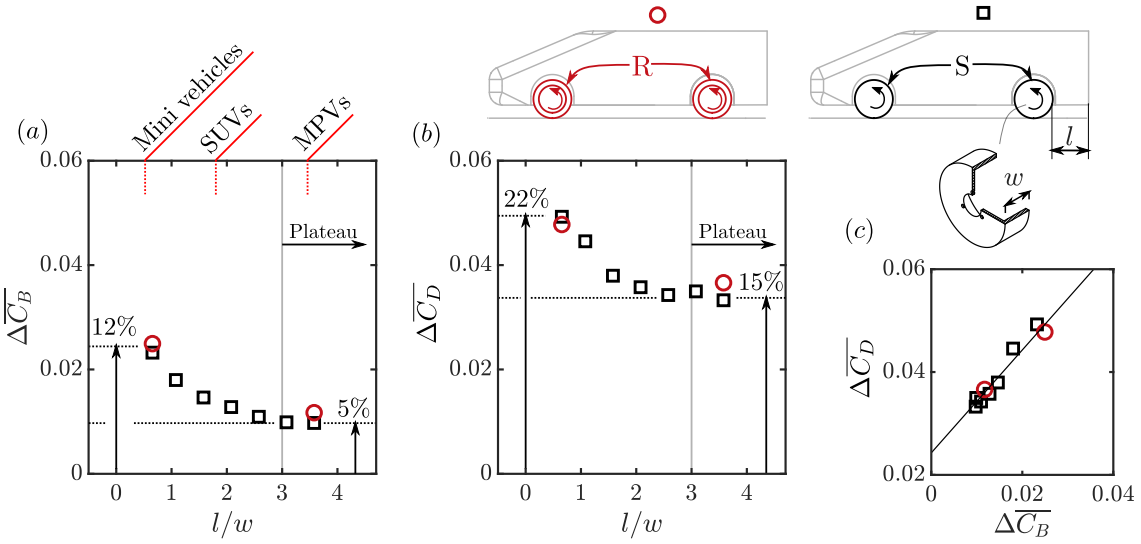

Figure 3: Evolution of (a) the base drag $\Delta\overline{C_B} = \overline{C_B} - \overline{C_{B0}}$ and (b) total drag $\Delta\overline{C_D} = \overline{C_D} - \overline{C_{D0}}$ of the body as a function of the wheel-to-base distance l/w. Both sharp-edged-shoulder wheels (S, colored in black) and rounded-shoulder wheels (R, colored in red) are considered. The relationship between $\Delta\overline{C_D}$ and $\Delta\overline{C_B}$ is shown in (c).

Preliminary Reynolds-Averaged Navier-Strokes (RANS) computations not shown here for brevity show that this base drag decrease with increasing vehicle length is a potential flow effect. Indeed, downstream the flow acceleration along the front part of the model and outside the boundary layer, in the potential flow region, the velocity at separation from the base decreases with vehicle length. This results in the observed pressure recovery. In what follows, when the wheels are installed, the base drag and total drag are always expressed relative to the corresponding baseline case with the same length in order to focus on the role of the wheels.

4. Salient features of wheel-vehicle interactions

4.1. Drag sensitivity to wheel-to-base distance

The global impact of the wheels on the baseline wake is now investigated. In figure 3(a) and (b), the base drag $\Delta\overline{C_B} = \overline{C_B} - \overline{C_{B0}}$ and total drag $\Delta\overline{C_D} = \overline{C_D} - \overline{C_{D0}}$ relative to the baseline cases are shown respectively. For each case having a base drag value of $\overline{C_B}$ and a total drag value of $\overline{C_D}$, $\overline{C_{B0}}$ and $\overline{C_{D0}}$ represent the values of the corresponding baseline case with the same vehicle length. A detailed measurement spanning all the possible wheel-to-base distances is conducted for the configuration using the sharp-edged-shoulder wheels S, while only the minimum and maximum l/w values are tested for the rounded-shoulder configuration R.

We focus first on the base drag variation in figure 3(a) for the configuration S. For the longest baseline case providing the maximum wheel-to-base distance max(l/w)=3.58, the wheels are found to increase the base drag by $\sim 5\%$ ($\Delta\overline{C_B}/\overline{C_{B0}} \approx 5\%$). With decreasing l/w, we remark that the base drag increase is very similar for $l/w = 3.58$ and $l/w = 3.08$. It is noted here that relative distances larger than $l/w = 3.58$ were not considered for the present study. However, by modeling the wheels as D-shaped obstacles, larger "wheel-to-base" distances were considered in Bao *et al.* (2022). A clear plateau having weak base drag sensitivity to the wheel-to-base distance was identified. In

what follows, we will therefore consider that a plateau is reached for $l/w > 3$. This will be further confirmed in section 5 by changing the initial wake balance.

By reducing the length of the vehicle, the wheel-to-base distance l/w is decreased. From $l/w = 3$ with decreasing l/w, a rapid quadratic increase in $\Delta\overline{C_B}$ is observed until the smallest l/w is reached, maximally leading to a base drag increase of $\sim 12\%$. This suggests the emergence of additional near-wake interactions between the rear wheels and the vehicle wake resulting in an extra base drag increase.

In figure 3(b), we consider the total drag acting on the whole vehicle model (wheel drag is not weighted). In the plateau, the drag increase from the baseline case is $\sim 15\%$. With decreasing l/w, the wheels maximally lead to a $\sim 22\%$ drag increase at the minimum l/w. The $\Delta\overline{C_D}$ evolution with l/w is very similar to the $\Delta\overline{C_B}$ evolution as shown before in figure 3(a) but presents an overall upward shift of ~ 0.024. The shift is due to the drag increase at the vehicle surfaces except at the base, for example the wheelhouse drag and/or the change in pressure at the front surfaces. More exactly, we observe that $\Delta\overline{C_D}(l/w) = 0.024 + \Delta\overline{C_B}(l/w)$ as depicted by showing the relationship between the total drag $\Delta\overline{C_D}$ and the base drag $\Delta\overline{C_B}$ in figure 3(c). This means that with variation in l/w, the base drag increase is the only source of total aerodynamic drag increase.

By comparing the configuration R with S in figure 3, it is shown that the base drag and total drag are not sensitive to the geometrical details of the wheels (wheel drag being not weighted). In particular, for the more realistic wheel shape R, we observe a slight increase of base drag at the plateau and the drag sensitivity with decreasing l/w. In what follows, comparisons of detailed measurements between the two configurations will be presented.

4.2. Global forcing of vehicle wake by the wheels

We first focus on the base pressure increase induced by the wheels for the longest body. By installing rotating wheels on a Windsor model, Pavia & Passmore (2017) have shown that the vehicle wake is modified from a well-balanced one to an asymmetric one dominated by a bottom recirculating flow. We therefore suspect the wheels to act as underflow perturbations modifying the global equilibrium of the wake. The largest wheel-to-base distance is considered here in order to focus on these global changes. The local interactions will be considered in the next section.

Barros *et al.* (2017) have shown that a systematic variation of the wake equilibrium can be induced by placing different kinds of perturbations in the underflow. In order to obtain a large span of wake orientations for the reference body (that is to say without rotating wheels), our choice is then to use the same strategy – see also Haffner *et al.* (2020, 2022); Legeai & Cadot (2020) - by placing a circular cylinder of varying diameter d (from $d/H = 0$ to 0.087) spanning the whole width of the baseline vehicle at $x/H = -1$ on either the top or bottom surface.

A large number of cases are selected in order to have a good description of the effect of global equilibrium modification on the reference body. Their joint p.d.f. and mean base pressure distributions are shown in figure 4(a). The whole bifurcation scenario with a competition between the vertical static asymmetry and the horizontal bi-modal asymmetry is observed. By increasing the size of the bottom (top) perturbing cylinder, the vertical asymmetry is gradually increased with a disappearance of the bi-modal dynamics of the baseline situation. The competition between these two asymmetries is then shown in figure 4(b) by the relationship between $\overline{z_b/H}$ and $\overline{|y_b/H|}$. For the baseline case and the cases perturbed by cylinder, the relationship follows approximately an elliptic shape, as pointed out by the elliptic model proposed by Bonnavion & Cadot (2018) and used in Lorite-Díez *et al.* (2020).

For three-dimensional wakes, these different asymmetries lead to important variations of base drag (see Grandemange *et al.* (2013) and Haffner *et al.* (2020) for different suggestions of the drag generation mechanisms). For an Ahmed body with a base aspect ratio of $H/W < 1$ similar to the present model, it is often measured that the wake presenting mean vertical symmetry and horizontal bi-stable asymmetry has the least base drag (Bonnavion & Cadot, 2018; Haffner *et al.*, 2020). The relationship between the vertical wake asymmetry $\overline{z_b/H}$ and the base drag variation caused by the cylinder $\Delta\overline{C_B}$ is shown in figure 4(c). It shows that the baseline case with small $|\overline{z_b/H}|$ presenting

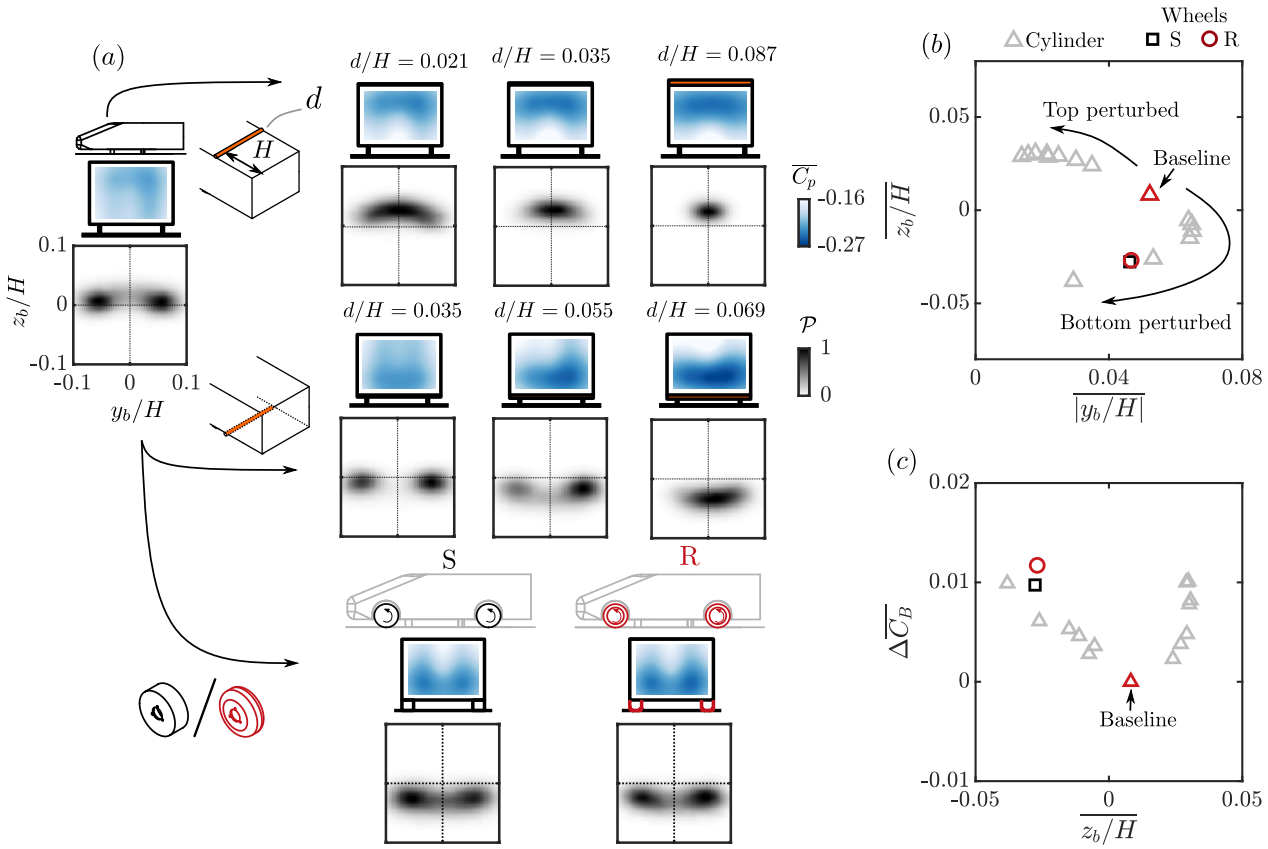

Figure 4: Longest baseline vehicle (wheel-to-base distance $l/w = 3.58$) perturbed either by spanwise cylinder or wheels. (a) Effect of spanwise perturbing cylinder or wheels on the base pressure distribution and joint p.d.f. of the base CoP position. S and R represent, respectively, sharp-edged-shoulder wheels and rounded-shoulder wheels. The cylinder of varying diameter d is placed horizontally at $x/H = -1$ on either the top or bottom surface of the vehicle. (b) Mean vertical position of the base CoP $\overline{z_b/H}$ versus mean absolute value of the horizontal base CoP position $\overline{|y_b/H|}$ for the baseline vehicle perturbed either by spanwise cylinder or wheels. (c) Base drag $\Delta\overline{C_B}$ versus $\overline{z_b/H}$ for the same cases in (b).

horizontal bi-modal dynamics has the least mean base drag. When the size of the top/bottom cylinder is increased and therefore the vertical asymmetry is enhanced, the base drag is increased by maximally 5%.

Having this database for the reference body, we are now in a position to examine the effect of the wheels. When the wheels, either S or R, are installed, it is shown in figure 4(a) that the mean base pressure distribution is modified from a relatively uniform one with vanishing vertical asymmetry to an uneven one with an obvious positive vertical pressure gradient. More generally, the mean value of the vertical CoP position $\overline{z_b/H}$ is decreased by the wheels. Meanwhile, it is noted that the base pressure distributions and the joint p.d.f. of the wheel cases are very similar to that of the $d/H = 0.055$ case. In figure 4(b), it is found that the wheel cases follow the relationship portrayed by the cylinder cases, indicating that the wheels play the same role as the underflow perturbing cylinder on the wake asymmetry. Focusing on figure 4(c) where the relationship between the vertical asymmetry and the base drag is discussed, we notice the wheel case follows approximately the trend measured using the cylinder.

The wake flow is now investigated in figure 5 to understand how the wake is modified by the wheels. In figure 5(a), the mean streamlines and turbulent kinetic energy k in the symmetry plane of the longest vehicle are presented. In accordance with the pressure measurements, the wheels, either type S or R, reorganize the structure of the mean vehicle wake, leading to a strong bottom-dominated recirculating flow. The wake reorganization increases the low-pressure imprint at the bottom part of the recirculating flow on the base. At the same time, the interaction mechanism in asymmetric wakes as proposed in Haffner *et al.* (2020) is enhanced by the growth of the upward

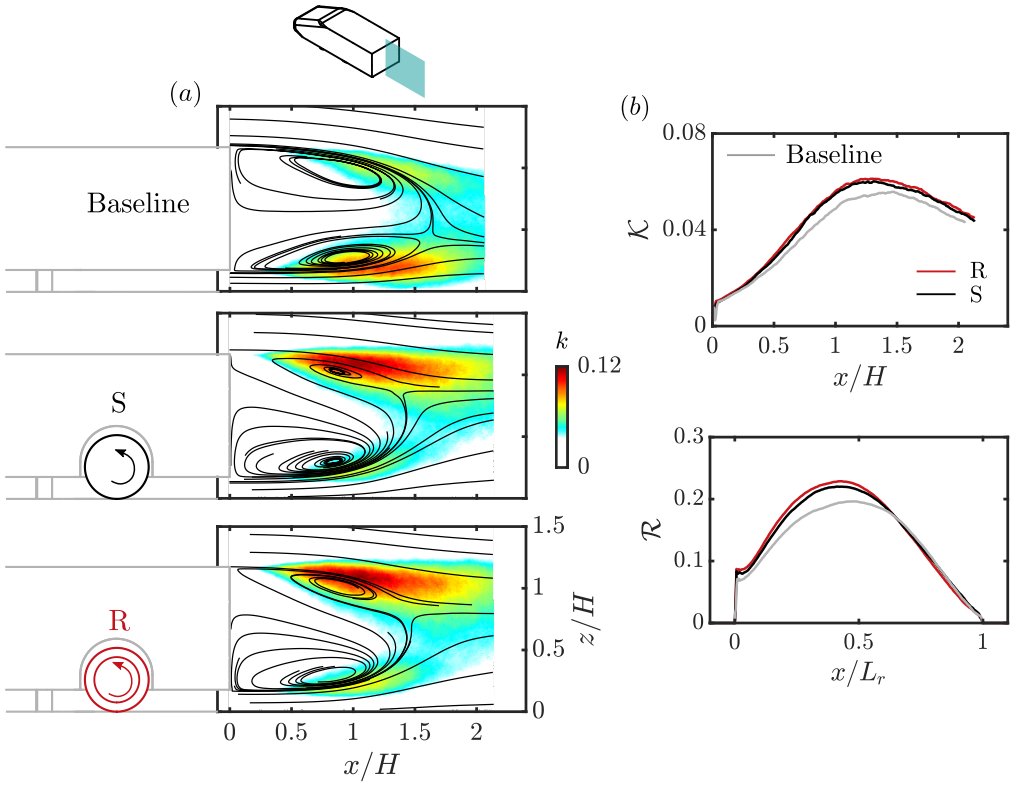

Figure 5: Effect of wheels on the wake of the longest baseline vehicle. S and R represent, respectively, sharp-edged-shoulder and rounded-shoulder wheels. (a) Mean streamlines superimposed on the turbulent kinetic energy k distribution. (b) Streamwise evolution of the integrated turbulent kinetic energy $\mathcal{K}$ and the recirculation strength R for the cases in (a), Gray lines represent the baseline case having no wheels.

cross-flow momentum, evidenced by the stronger flow fluctuation in the top shear layer. This aspect is shown in figure 5(b) by integrating the turbulent kinetic energy k across the measurement plane:

$$\mathcal{K}(x) = \int_0^{z_{max}} k(x,z)dz. \tag{7}$$

This quantity reveals the global enhancement of the turbulent fluctuation in the wake. It leads to changes in the intensity of the recirculating flow, which is quantified by defining a quantity:

$$\mathcal{R}(x) = \int_{\overline{u_x}\leq 0} \sqrt{\overline{u_x}^2 + \overline{u_z}^2}dz, \tag{8}$$

As shown in figure 5(b), the wheels, either type S or R, lead to an overall enhancement of the recirculating motion from the baseline case, with the maximum of the recirculating strength $\mathcal{R}$ increases by $\sim 12\%$. This enhancement produces a lower pressure at the center of the recirculation region in accordance with the lower pressure footprint measured on the base.

4.3. Near-wake interactions for small wheel-to-base distance

In this section, the investigation is focused on the flow mechanisms resulting in the $\Delta\overline{C_B}$ increase with decreasing l/w for $l/w < 3$. It is important to note here that the global forcing of the vehicle wake found in the last section is also measured for all the l/w cases in this section.

We start by examining in figure 6(a) the base pressure distribution for the longest vehicle ($l/w = 3.58$) and the shortest vehicle ($l/w = 0.65$). On the right-hand side of the base, the distribution of pressure difference $\Delta\langle\overline{C_p}\rangle$ with respect to the corresponding baseline case is also shown for comparison. For both configurations S and R, the base pressure decreases when l/w is reduced. The portion of the base that contributes to the increase in $\Delta\overline{C_B}$ can be obtained by comparing the $\Delta\langle\overline{C_p}\rangle$ distributions. A decrease in $\Delta\langle\overline{C_p}\rangle$ in observed at the bottom half of the base

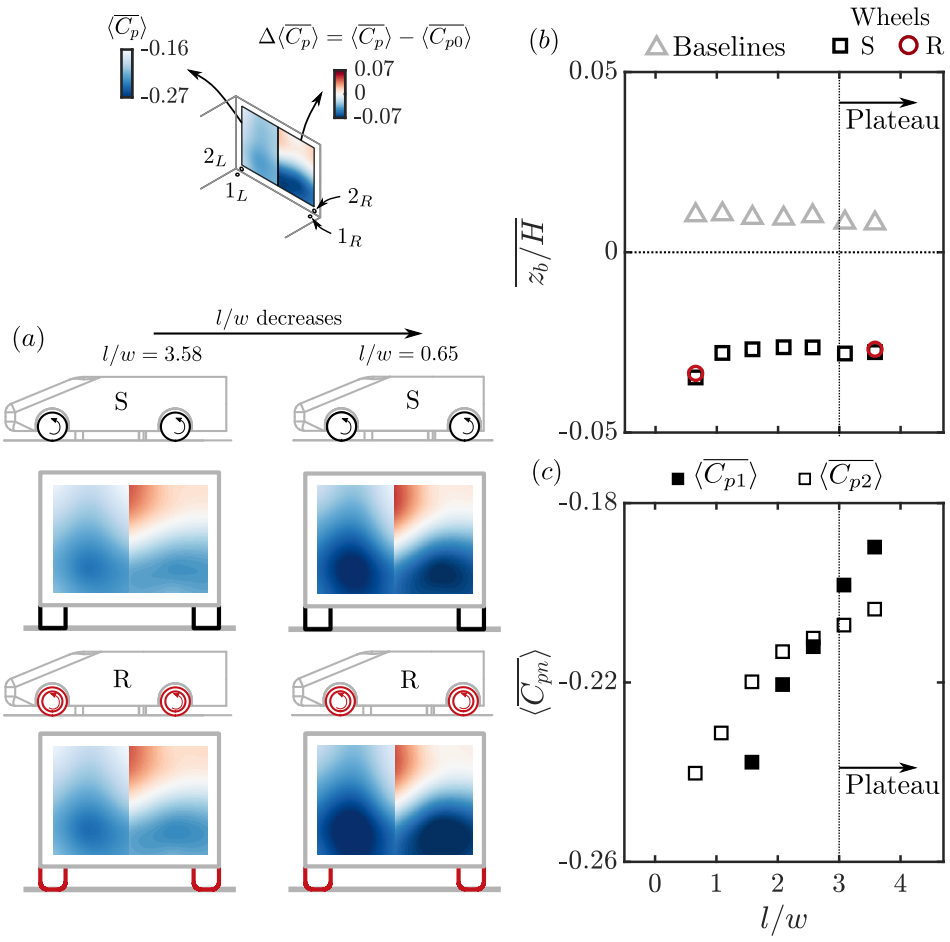

Figure 6: Effect of the reduction in the wheel-to-base distance l/w on the base pressure. S and R represent, respectively, sharp-edged-shoulder and rounded-shoulder wheels. (a) Base pressure distributions for the smallest and the largest l/w cases, the mean values and the differences with respect to the corresponding baseline case are respectively presented at the left-hand and right-hand sides of the base. (b) Evolution of the mean vertical position of the base CoP $\overline{z_b/H}$ with l/w, the values for the baseline cases (no wheels) are shown for comparison using triangles. (c) Comparison between the evolution of $\langle\overline{C_{p1}}\rangle$ and $\langle\overline{C_{p2}}\rangle$, the location of the pressure taps are schematically shown above (a).

near the rear wheels. This region of base pressure decrease is also illustrated in figure 6(b) by the continuous decrease in $\overline{z_b/H}$ with decreasing l/w at $l/w < 3$.

Now the pressure in the vicinity of the rear wheels is considered. The pressure measurements at the taps numbered 1_L and 2_L (1_R and 2_R), located in the symmetry plane of the left-hand (right-hand) side wheels (see the sketch in figure 6), are used for a comparison in figure 6(c). These pressure taps are located on both sides of the bottom trailing edge, representing the pressure levels behind the rear wheels and at the base near the rear wheels. It should be noted here that the taps numbered 1 are always located at $x/H = -0.07$ for different vehicle lengths. For the shorter cases $l/w = 0.65$ and 1.58, pressure taps 1_L and 1_R are not available due to mechanical constraints. In the plateau ($l/w > 3$), $\langle\overline{C_{p1}}\rangle$ is higher than $\langle\overline{C_{p2}}\rangle$. For a canonical separating flow, the pressure condition at separation is similar to the observation here with the separating streamline inducing a lower pressure inside the recirculation region (Bradshaw, 1973). On the other hand, in the drag-sensitive regime $l/w < 3$, $\langle\overline{C_{p1}}\rangle$ is lower than $\langle\overline{C_{p2}}\rangle$. The difference $\langle\overline{C_{p2}}\rangle - \langle\overline{C_{p1}}\rangle$ increases with decreasing l/w.

These observations point out the close relationship between the pressure decrease at the model base and the increasing influence from the rear wheels when the wheel-to-base distance l/w is decreased in the drag-sensitive regime $l/w < 3$. The streamwise development of the rear wheel wake is therefore of particular importance here. We then define a new reference frame in figure 7(a) in order to examine this. The rearmost location of the part of the rear wheels exposed to

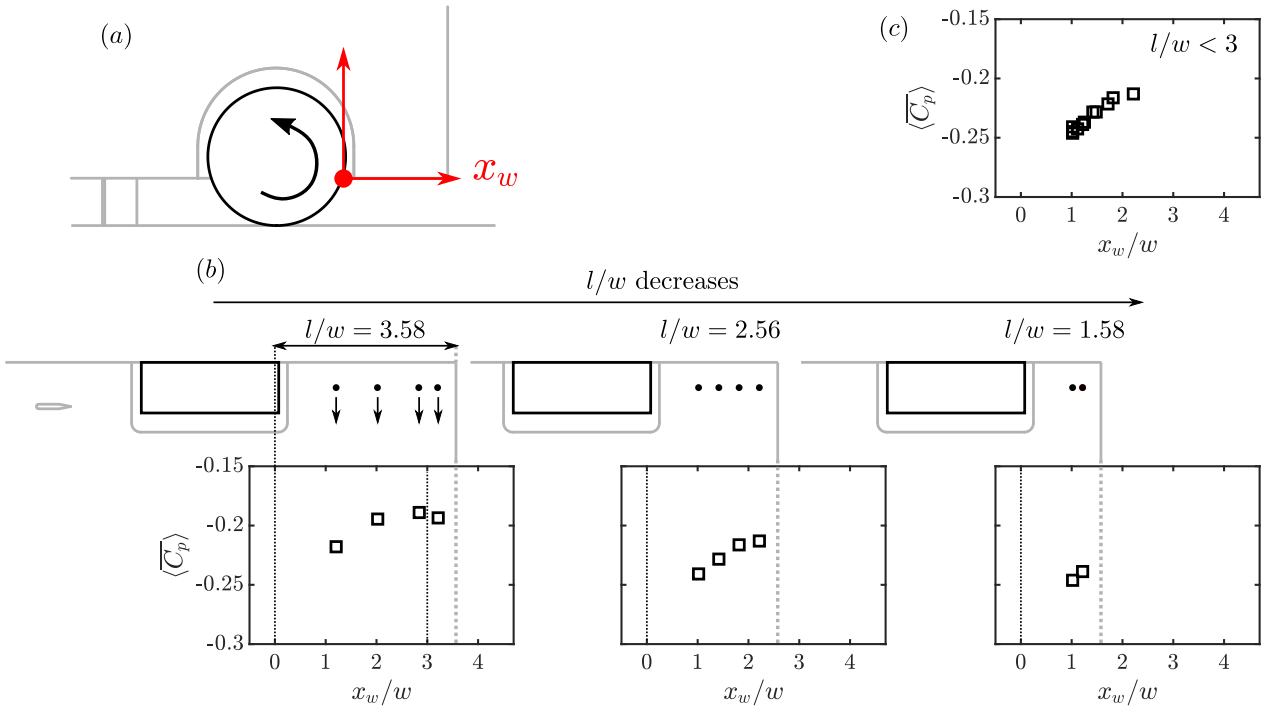

Figure 7: Streamwise pressure evolution in the wake of the rear wheels (sharp-edged-shoulder ones). (a) Definition of a wheel-fixed coordinate system. (b) Evolution of $\langle \overline{C_p} \rangle$ as a function of x_w for three different l/w cases. (c) Superposition of the $\langle \overline{C_p} \rangle$ evolution for all the cases in the drag-sensitive regime $l/w < 3$.

the underflow is set as the origin of this frame with $x_w = 0$. For each l/w case, as shown in the sketch in figure 7(b), several pressure taps are located under the vehicle in the symmetry planes of the rear wheels. These pressure measurements are plotted against the distance from the measurement location to the rear wheels x_w in figure 7(b). Only S configuration is presented for brevity. For case $l/w = 3.58$ ($\max(l/w)$), a rapid pressure increase with increasing x_w/w is measured at $x_w/w < 3$ which corresponds to the near-wake region of the rear wheels. For decreasing l/w, the bottom trailing edge of the vehicle approaches the rear wheels and is gradually influenced by the near-wake region of the rear wheels. This is the reason for the decrease of $\langle \overline{C_{p1}} \rangle$ in the drag-sensitive regime $l/w < 3$. For all the cases in the drag-sensitive regime ($l/w < 3$), the streamwise pressure developments are gathered together in figure 7(c). It is found that all these cases collapse approximately on the same evolution. This means that the wakes of the rear wheels keep their mean properties in the drag-sensitive regime when l/w is varied. Again, we notice a decrease in pressure with decreasing x_w/w at $x_w/w < 3$.

Noticeably, the bottom trailing edge of the vehicle experiences a gradual increase of periodic dynamics with decreasing l/w, which is captured by the unsteady pressure sensors numbered 1 and 2. The evolution with l/w of the premultiplied spectra of the pressure signals obtained from the pressure taps 1 and 2 are shown in figure 8(a) and (b). Pressure sensors 1 measure a rapid growth in energy at $St_w = fw/U_0 = 0.15$ (here w is the width of the wheels) with decreasing l/w in the range $l/w < 3$. This growing influence of the wheel wake dynamics is also observed at the base (see figure 8b). It is noted here that Croner *et al.* (2013) experimentally measured a peak at $St_w = 0.14$ downstream an isolated rotating wheel wake. With the help of numerical simulations, they found the same peak in the spectrum of the side force. Recently, this St_w was also measured by Patel *et al.* (2022). Therefore, the peak measured in the present study may represent the horizontal periodic motion of the rear wheel wake. Finally, a peak at a relatively low frequency, about $St_w = 0.022$ (corresponding to $St_W = fW/U_0 = 0.16$, where W is the width of the vehicle), is measured at the base. This frequency matches with the horizontal periodic dynamics of the vehicle wake measured for example in Grandemange *et al.* (2013) and Lorite-Díez *et al.* (2020). For configuration R, figure 8(c) shows the premultiplied spectrum of the pressure signal obtained from the pressure taps 2. We observe the same evolution as in figure 8(b) for configuration S. The low-frequency peak at

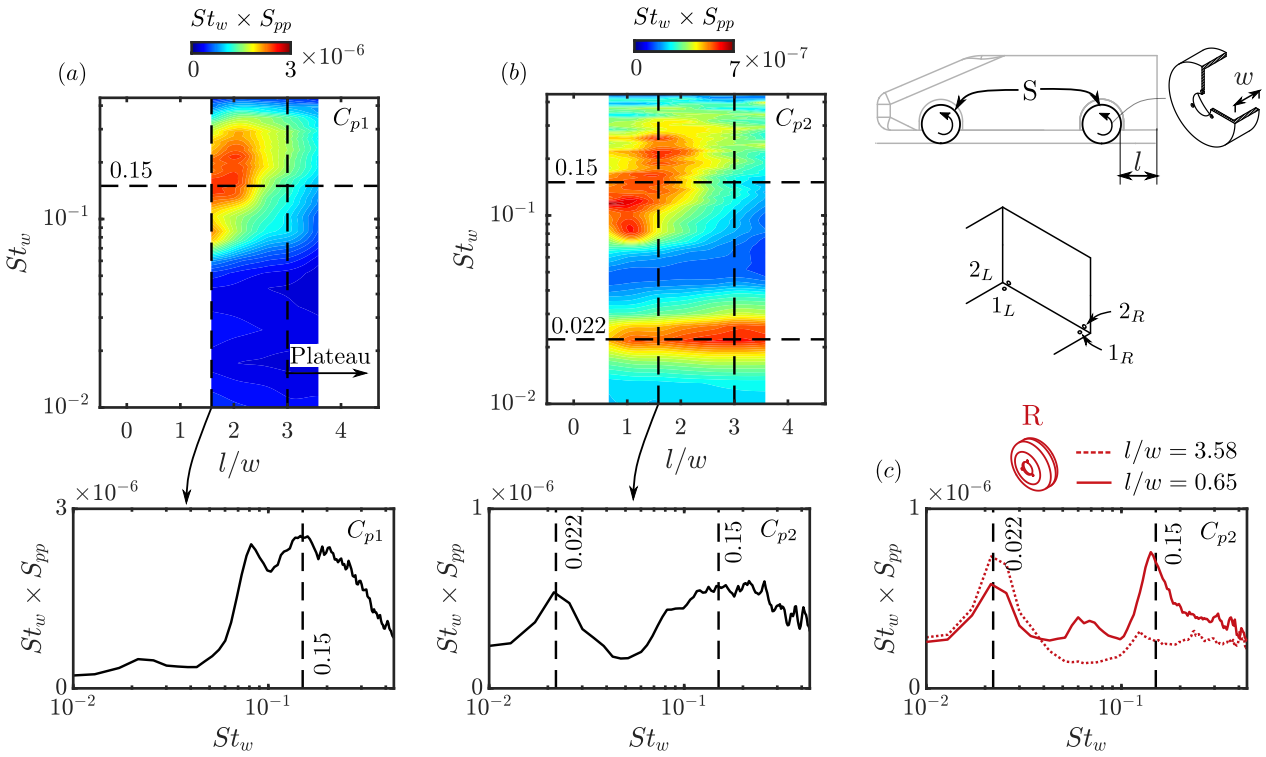

Figure 8: For configuration S: evolution of the premultiplied spectra of C_{p1} (a) and C_{p2} (b) with the wheel-to-base distance l/w. At $l/w = 1.58$, the spectra are also shown. For configuration R: premultiplied spectrum of C_{p2} (c) for the maximum and the minimum l/w.

$St_w = 0.022$ driven by the vehicle wake, is observed in both situations $l/w = 3.58$ and 0.65. The signature of the wheel wake dynamics at $St_w = 0.15$ is only detected for $l/w = 0.65$.

The velocity fields are investigated in order to understand the modifications in the vehicle wake and to reveal the flow mechanisms responsible for the $\Delta\overline{C_B}$ increase with decreasing l/w for $l/w < 3$. The streamwise velocity $\overline{u_x}$ downstream the vehicle is presented in figure 9(a). Similar mean velocity fields obtained for rounded-shoulder wheels are not shown for brevity. First of all, in the symmetry plane of the vehicle $y/H = 0$, no obvious change in the wake topology is noticed. However, by integrating the flow momentum inside the recirculation region, the recirculation strength $\mathcal{R}$ shows an important change in figure 9(b). From $l/w = 3.58$ to $l/w = 0.65$, the maximum of $\mathcal{R}$ is increased by $\sim 12\%$. This is valid for both configurations S and R, between which only slight differences are noticed.

Local velocity measurements shown in figure 9(a), downstream of the left-hand wheels, reveal a more pronounced difference between the cases. In the symmetry plane of the left-hand wheels, the streamwise velocity $\overline{u_x}$ below the vehicle wake is lower for $l/w = 0.65$ than $l/w = 3.58$. This reduces significantly the mean shear between the vehicle wake and the wakes of the rear wheels as illustrated in figure 9(c) by plotting the $\overline{u_x}$ distributions along $x/H = 0.03$ in this plane. It is shown that no matter the type of wheels, the decrease of l/w always reduces the mean shear between the vehicle wake and the wakes of the rear wheels.

Along with the mean shear strength with reducing l/w, an important remark is that a mean mass transfer from the vehicle wake to the wakes of the rear wheels is observed. In figure 10, the mass transfer is illustrated by the distribution of the mean vertical velocity $\overline{u_z}$ in the symmetry plane of the left-hand wheels for the same cases as in figure 9(a). A clear difference is found near the base of the vehicle. For the $l/w = 0.65$ case, there is a downward motion from the recirculation region of the vehicle toward the ground indicated by an overall negative $\overline{u_z}$ in the flow downstream of the rear wheel. This feature is not observed for the $l/w = 3.58$ case. The difference is better illustrated by plotting the distribution of $\overline{u_z}$ along $x/H = 0.03$ in figure 10(b) for both the configurations S and R. For the cases $l/w = 3.58$, we notice a sharp change in $\overline{u_z}$ at the location of the shear $z/H = G/H$ with different signs above and below this location. On the other hand, case $l/w = 0.65$ always

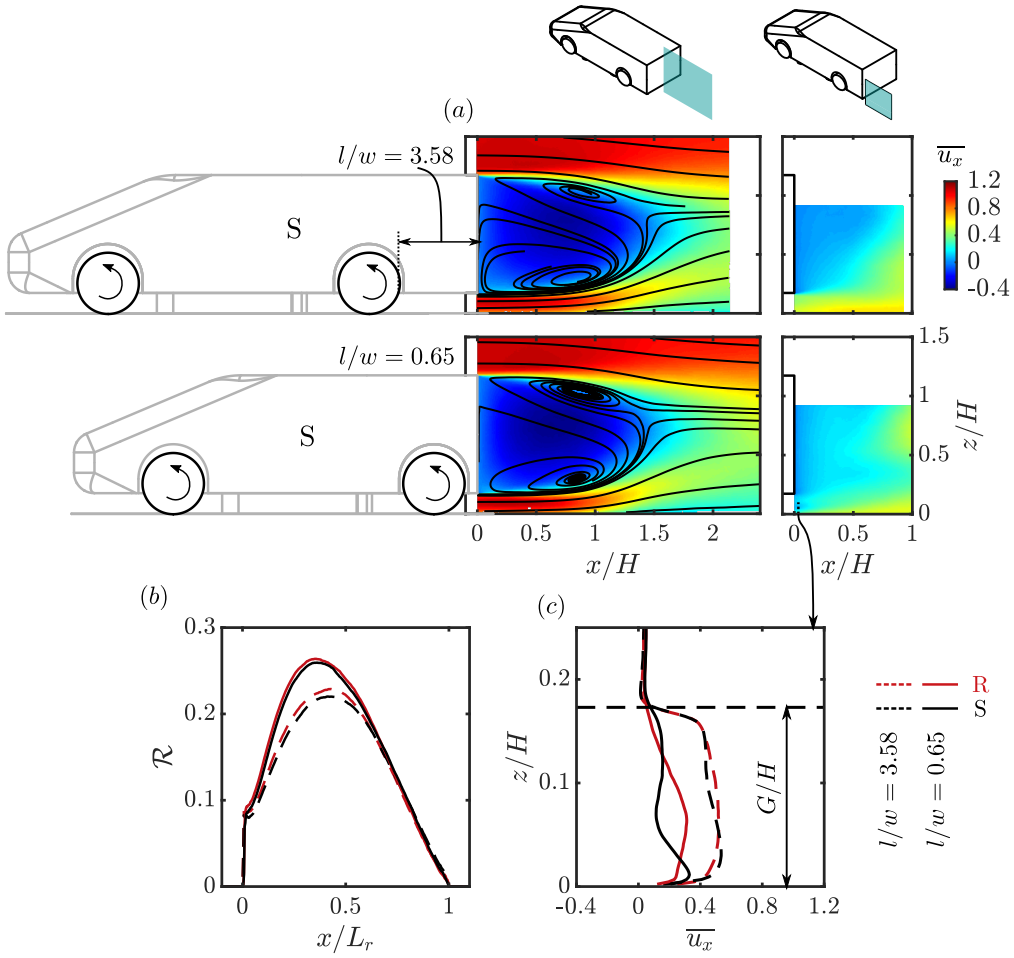

Figure 9: Effects of l/w reduction from the maximum l/w ($l/w = 3.58$) to the minimum l/w ($l/w = 0.65$) on the mean flow downstream of the vehicle. S and R represent, respectively, sharp-edged-shoulder and rounded-shoulder wheels. (a) Distributions of mean streamwise velocity $\overline{u_x}$ in the symmetry plane of the vehicle at $y/H = 0$ and of the left wheels at $y/H = -0.58$ for the configuration S. (b) Recirculation strength $\mathcal{R}$ for the configurations S and R. (c) $\overline{u_x}$ profiles along $x/H = 0.03$ in the symmetry plane of the left wheels for the configurations S and R.

present a negative $\overline{u_z}$ near $z/H = G/H$.

The streamwise span of the mean mass transfer is quantified in figure 10(c) by plotting the mean vertical velocity $\overline{u_z}$, at the ground clearance height G/H, as a function of either the distance from the base x/H or the distance from the rear wheels x_w/w. The length of the mass exchange interface approximately ends at $x_w/w = 3$. It is reminded here that this region behind the rear wheels with $x_w/w < 3$ was shown to experience a lower pressure than the wake of the vehicle (see figure 6c). With variation in l/w, the length of the region is not expected to be modified since the pressure in the rear wheel wake is measured to be not changed in figure 7(c). The physical picture is thus that the rear wheel wakes impose a lower static pressure and a downstream region having the ability to induce mass exchange from the main wake of the vehicle. With the length of this region of order $x_w/w = 3$, a decrease of the wheel-to-base distance l/w then induces a higher mass transfer and a larger drag increase. Further comments on the relation between the mass transfer and the base drag sensitivity are provided in appendix B by adapting the model of Bao *et al.* (2022).

For the $l/w = 0.65$ case, additional velocity measurements at $x/H = 0.03$ are shown in figure 11(a) to show the flow structures generated by the wheels and to provide the information of mass exchange in the horizontal direction of the interaction interface. The distributions of the mean velocity magnitude $\overline{U}$ are shown for the two cases S and R. In figure 11(a), we see clearly several flow regions that experience a deficit of mean longitudinal momentum. The wake of the left-hand rear wheel has the same velocity level as the recirculation region behind the vehicle. Another region

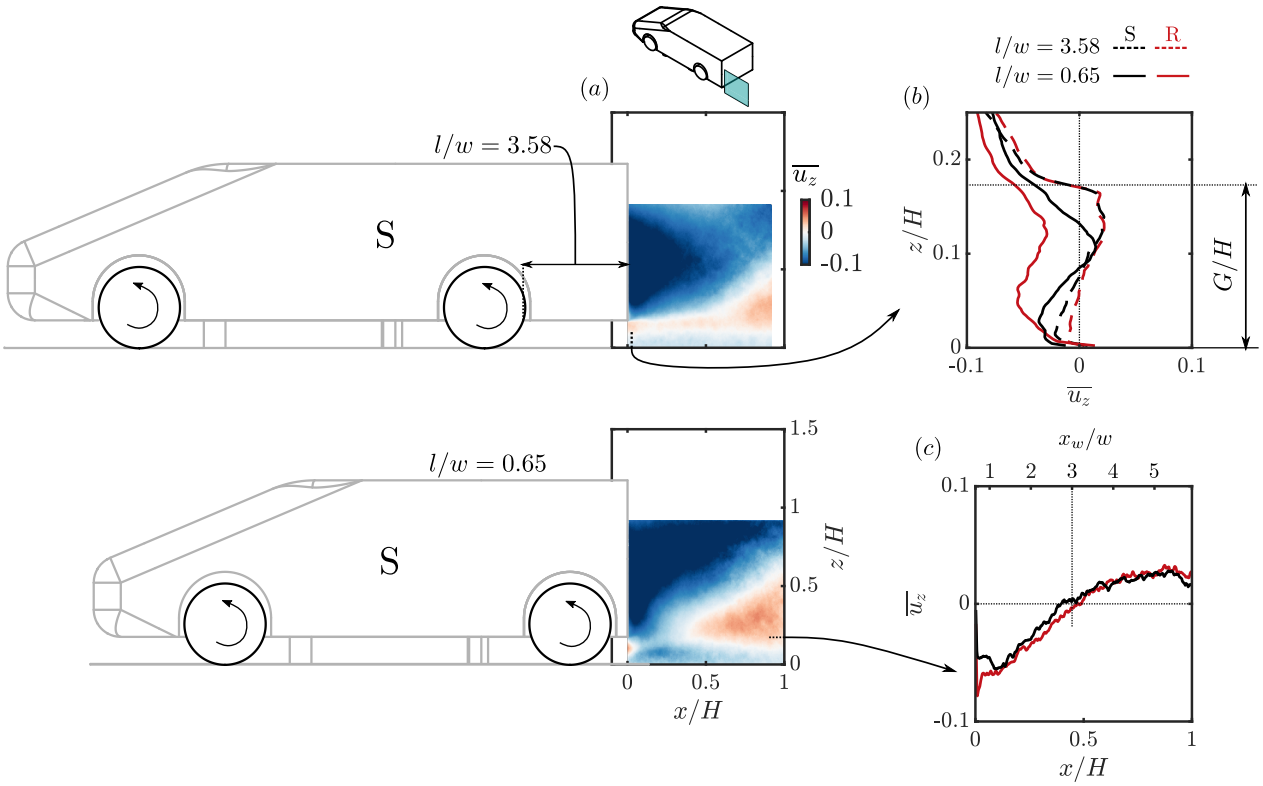

Figure 10: (a) Effect of l/w reduction on the mean vertical velocity $\overline{u_z}$ in the symmetry plane of the left-hand wheels for the configuration S (sharp-edged-shoulder wheels). (b) Vertical profiles of $\overline{u_z}$ at $x/H = 0.03$ for the two configurations S and R (rounded-shoulder wheels). (c) $\overline{u_z}$ distributions at the height of the ground clearance $z/H = G/H$ for the $l/w = 0.65$ cases of the two configurations.

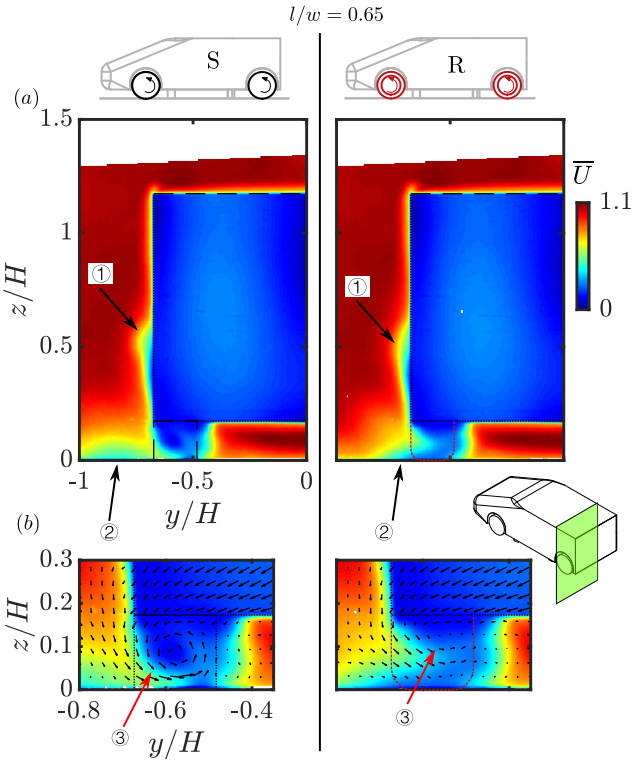

Figure 11: For the shortest vehicle case $l/w = 0.65$: (a) Mean streamwise $\overline{u_x}$ velocity distributions in the cross-flow plane at $x/H = 0.03$, S and R represent, respectively, sharp-edged-shoulder and rounded-shoulder wheels. (b) Zoom views of the cases in (a) superimposed by in-plane mean velocity vectors.

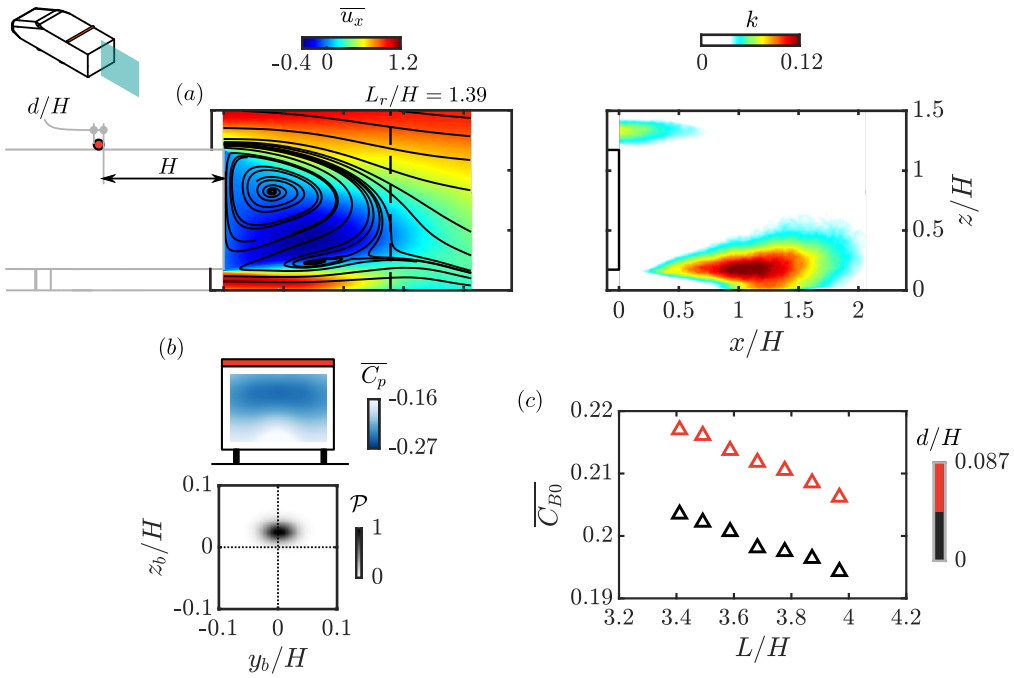

Figure 12: Baseline flow for the longest vehicle $L/H = 3.97$ perturbed by a circular cylinder $d/H = 0.087$ at $x/H = -1$ on the top surface. (a) Mean streamwise velocity $\overline{u_x}$ and turbulent kinetic energy k in the symmetry plane of the vehicle $y/H = 0$. (b) Mean base pressure distribution and the Joint probability density function (p.d.f.) of the base CoP position. (c) Evolution of the base drag $\overline{C_{B0}}$ with the length of the vehicle L/H, the baseline cases from figure 2 with $d/H = 0$ are shown for comparison.

(marked by ①) is observed for both configurations S and R behind the rear wheelhouse. A third region (marked by ②), is situated at the left-hand side of the wheel. This region is clearly visible for configuration S while for configuration R it is closer to the left-hand shear layer of the wheel. When looking closer at the flow behind the wheel in figure 11(b), a counter-clockwise mean streamwise vortical structure (marked by ③) is depicted by the in-plane mean velocity vectors. This structure is noticed for both configurations and appears to be less intense for configuration R than for S. In addition, the velocity vectors at the height of the ground clearance show that the mass transfer is always from the vehicle wake to the wakes of the rear wheels. The span of the mass exchange surface in the spanwise direction is approximately the width of the wheel.

We now compare the wheel wake structure in the present work with that in previous studies. The experimental measurements behind the front wheel of a car model in Wäschle (2007) are selected for the comparison (see figure 7c in Wäschle (2007)). A moving ground facility was used and the wheels are solid due to the small scale of the model. Recently in Josefsson *et al.* (2022*b*), the measurements were confirmed by a combination of experiments and numerical simulations using deformable tires. The measurement plane was located at $0.6d_w$ downstream of the wheel axle, where d_w represents the diameter of the wheel. In our study, the measurement plane is located at $0.8d_w$ downstream of the wheel axle. First, the two regions of momentum loss ① and ② were measured. In Wäschle (2007), additional numerical simulations were able to reveal that two streamwise vortical structures are the reasons for the momentum loss regions. In addition, the vortical structure ③ behind the wheel was measured with the same rotation direction as the present work. Finally, the present work is found also in accordance with the vortex skeleton model proposed by Regert & Lajos (2007) using RANS simulations and confirmed by Krajnović *et al.* (2011) based on Large-eddy simulations.

5. Influence of initial asymmetry of the baseline wake

In this section, we examine the wheel-vehicle interactions based on a different baseline wake. This baseline wake is derived from the previous one by placing a perturbing cylinder having a diameter of $d/H = 0.087$ on the top surface (at $x/H = -1$, see section 4.2) for the seven different vehicle lengths

L/H	3.41	3.49	3.59	3.68	3.78	3.87	3.97
$\overline{C_{B0}}$	0.217	0.216	0.214	0.212	0.211	0.209	0.206
$\overline{C_{D0}}$	0.295	0.298	0.295	0.295	0.294	0.292	0.292

Table 4: Evolution of the mean aerodynamic coefficients with the model length L.

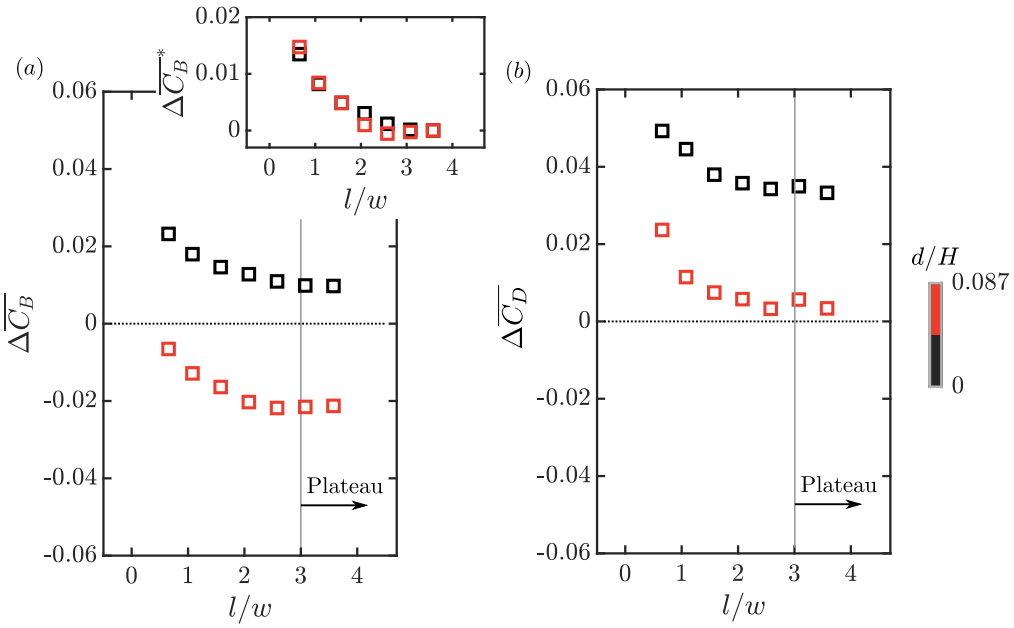

Figure 13: Based on a different baseline wake (top perturbing cylinder $d/H = 0.087$ used here): (a) Base drag $\Delta\overline{C_B} = \overline{C_B} - \overline{C_{B0}}$ and (b) total drag $\Delta\overline{C_D} = \overline{C_D} - \overline{C_{D0}}$ of the vehicle perturbed by sharp-edged-shoulder wheels as a function of the wheel-to-base distance l/w, the base drag varient $\Delta\overline{C_B}^* = \Delta\overline{C_B} - \Delta\overline{C_B}(max(l/w))$ versus l/w is also shown in (a).

L/H. A picture of this baseline flow is presented in figure 12(a) by showing the measurements for the longest vehicle. It is found that the cylinder alters the vehicle wake from a well-balanced one to a vertical asymmetric one dominated by a top recirculating flow. This is shown by both the mean streamlines and the turbulent kinetic energy k in the symmetry plane of the vehicle. In addition, the horizontal bi-modal dynamics of the wake is inhibited and the wake is locked to a vertical static asymmetric state. The aim of introducing such an asymmetric baseline wake is to generalize the findings described previously, since the wakes of square-back road vehicles present different vertical asymmetries. The mean base drag $\overline{C_{B0}}$ and total drag $\overline{C_{D0}}$ coefficients are displayed in table 4. The increase in base drag with decreasing vehicle length L/H is again observed for this baseline (also plotted in figure 12c).

The sharp-edged-shoulder wheels S are then tested on the present baseline. The effects on the base drag $\Delta\overline{C_B} = \overline{C_B} - \overline{C_{B0}}$ and on the total drag $\Delta\overline{C_D} = \overline{C_D} - \overline{C_{D0}}$ are shown respectively in figure 13(a) and (b). The results discussed before in the previous sections (named as $d/H = 0$) are presented for comparison. It is shown in figure 13(a) that the $\Delta\overline{C_B}$ evolution for the new configuration presents an overall downward shift. The wheels now play an opposite role on the base drag in the plateau with a base drag decrease of $\sim 9\%$. From the plateau with decreasing l/w, the same evolution as that of the $d/H = 0$ configuration is observed. This is evidenced by defining a variant of base drag variation $\Delta\overline{C_B}^* = \Delta\overline{C_B} - \Delta\overline{C_B}(\max(l/w))$, where the two curves collapse approximately. When the total aerodynamic drag is considered in figure 13(b), an overall upward shift of ~ 0.024 from the $\Delta\overline{C_B}$ evolution in figure 13(a) is noticed. This is similar to the $d/H = 0$ configuration.

An examination of the mean wake flow is presented in figure 14. The global modifications of the vehicle wake by the wheels are exemplified using the case with the longest vehicle in figure 14(a). In contrast to the increase in wake asymmetry observed before for the $d/H = 0$ configuration in figure

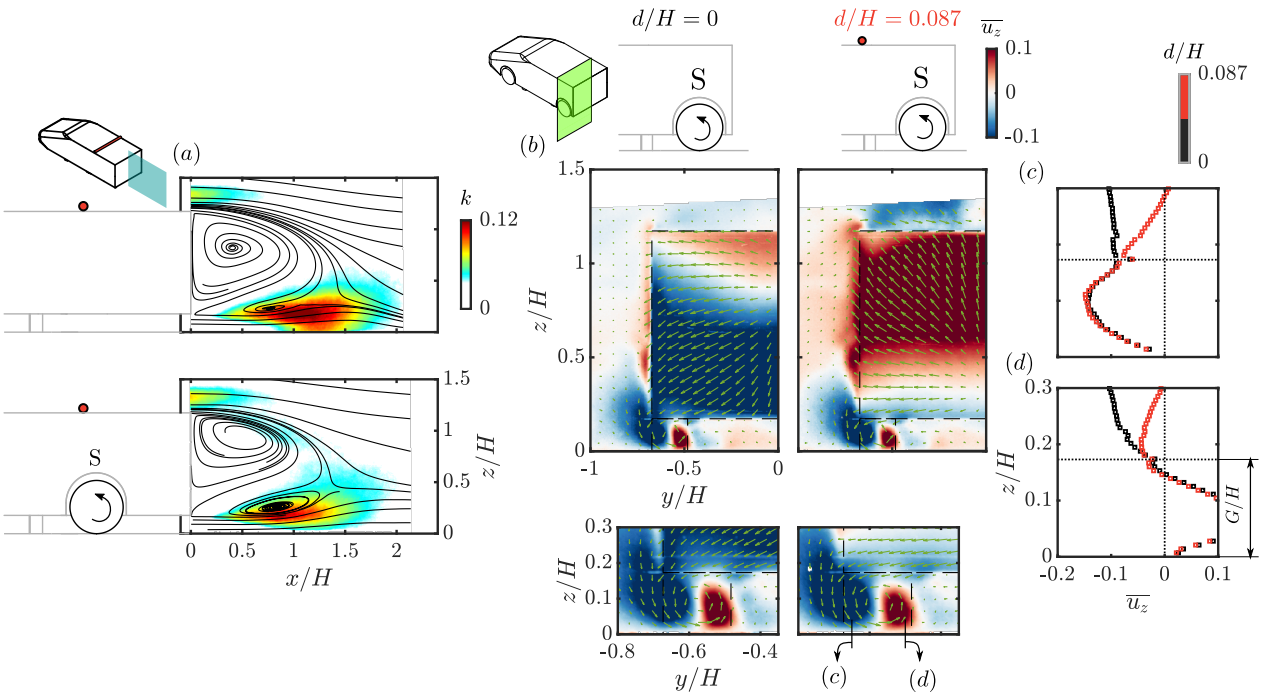

Figure 14: (a) Effect of sharp-edged-shoulder wheels on the longest baseline wake, the vehicle is perturbed with a $d/H = 0.087$ cylinder at the top. (b) For the shortest vehicle with sharp-edged-shoulder wheels: evolution of the mean vertical velocity $\overline{u_z}$ with the size of the top-perturbing cylinder d in the cross-flow plane $x/H = 0.03$, the vertical profiles at $y/H = -0.64$ and -0.52 are shown respectively in (c) and (d).

$5(a)$, here we measure a symmetrization of the vehicle wake as shown by the mean streamlines and the lower turbulent kinetic energy k in the bottom shear layer.

On the other hand, with decreasing l/w, the $\Delta\overline{C_B}$ increase is also accompanied by the emergence of the mass exchange between the rear wheel wakes and the vehicle wake for the $d/H = 0.087$ configuration. This is shown in figure $14(b)$ by comparison with the $d/H = 0$ configuration. The $\overline{u_z}$ distributions at $x/H = 0.03$ for the shortest vehicle are presented. Inside the vehicle wake, the recirculating flow is very different for these two configurations. However, the mass exchange velocity at the interface $z/H = G/H$ is not varied significantly. This is depicted by plotting the $\overline{u_z}$ profiles at $y/H = -0.64$ and -0.52, respectively, in figures $14(c)$ and (d). Despite the very different $\overline{u_z}$ distributions in the vehicle wake ($z/H > G/H$), the mean vertical velocity $\overline{u_z}$ at $z/H = G/H$ is of the same level for the two configurations.

These results show clearly that wheels have two different effects. On one hand, at the scale of the vehicle, they induce a global variation of the wake balance which, according to the initial state of the wake, increases or reduces the global drag (note for example that adding wheels is always beneficial for the base drag of the vehicle perturbed by the cylinder). On the other hand, for moderate wheel-to-base distances, a local interaction driven by the wakes of the wheels takes place. This interaction induces a mass transfer from the main wake and is responsible for a drag increase.

6. Concluding remarks

A road vehicle is a complex multi-scale geometry and all flow regions are interacting. Salient features of wheel–vehicle interactions and their consequences for drag were considered in this paper. At first order, we have shown that two different mechanisms can be distinguished, tentatively sketched in figure 15. At the scale of the vehicle, wheels perturb the underflow and induce a global variation of the vertical balance of the wake (I in figure 15). According to the state of the initial wake, significant base drag increase or decrease is observed. Considering now the scale of the wheels, we have shown that the wake region of the rear wheels imposes a low static pressure having the ability to induce a mean mass exchange from the main wake of the vehicle to the wakes of the rear wheels if the wheel-to-base distance is smaller than a threshold of order $3w$ (w is the width of the wheels) in

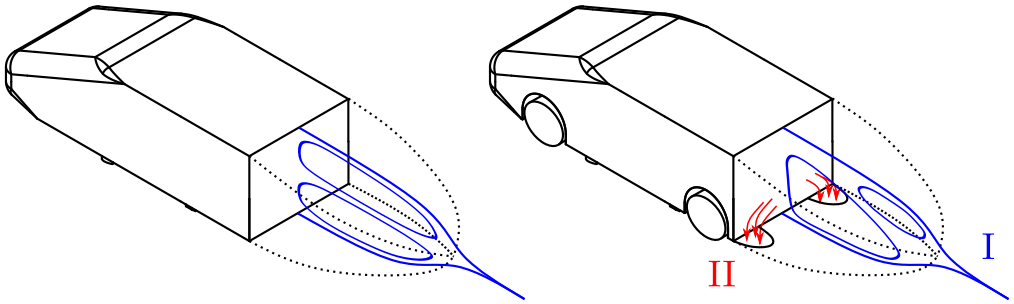

Figure 15: A conceptual sketch of the two flow mechanisms of wheel-vehicle interactions responsible for base drag variations. I: global variation of the vertical balance of the vehicle wake. II: mean mass exchange from the wake of the vehicle to the wakes of the wheels.

the present situation (II in figure 15). A constant mean mass flux extracted from the recirculation region means that this mass flux has to continuously enter the recirculation region of the vehicle wake and that the corresponding fluid particles have lost their mean longitudinal momentum. The physical model proposed in Bao *et al.* (2022) is used in appendix B to link mass exchange and base drag increase and to check the consistency of the measurements.

While these two mechanisms for wheel–vehicle interactions are of course coupled at the scale of the vehicle, we insist on the fact that they do have to be distinguished because they imply different physical processes. Moreover, for different initial states of the wake selected for example in section 5, it is interesting to figure out that the evolution with the wheel-to-base distance of the base drag increase due to mean mass transfer is very similar in both situations – see insert in figure 13(a). This means that the local characteristics of the wake of the wheels dominate this contribution to the base drag.

In general, the physical mechanisms highlighted here provide some guidelines for the drag reduction of ground vehicles. For different vehicle geometries having different wake asymmetries, reducing the wheel drag and minimizing the mean mass transfer are always favorable. However, after any local changes at the scale of the wheels, one should search for the optimum wake balance for this particular configuration. This can be obtained by modifying the angle of the rear spoiler or the diffuser for example. Further experiments are on their way to study different vehicle geometries and the role of interactions between the front and rear wheels.

Acknowledgements. The authors would like to warmly thank M. Grandemange from MFP Michelin and Y.Haffner from CSTB for insightful discussions, J.-M. Breux for invaluable support during the experiments, as well as F. Paillé, P. Braud and R. Bellanger for assistance with the PIV system.

Funding. The authors are deeply indebted for the support from MFP Michelin and the CPER Feder programme Transport of Région Nouvelle-Aquitaine. D.B. wishes to acknowledge the support from China Scholarship Council (CSC No. 201806260262).

Declaration of interests. The authors report no conflict of interest.

Appendix A. Effects of wheel state: rotating or stationary

In the present study, the wheel-vehicle interactions are investigated using rotating wheels. It is important to question if the conclusions of the present study hold, at least qualitatively, for the configuration with stationary wheels. By repeating the measurements presented in figure 3 but with stationary wheels, we examine in figure 16 the effects of wheel state.

In figure 16(a), the effect of wheel state on the base drag is presented. The two different wheel types, S and R, are considered. For different wheel-to-base distances l/w, the base drag increases slightly for fixed wheels. The base drag increase is the same for all the l/w distances. In figure 16(b), the total drag $\Delta\overline{C_D}$ is presented. For stationary cases, figure 16(c) shows $\Delta\overline{C_D}(l/w) = 0.036 + \Delta\overline{C_B}(l/w)$. The upward shift of ~ 0.036 is bigger than ~ 0.024 for the rotating wheels.

The insensitivity of the base drag to the wheel state is in accordance with the measurements

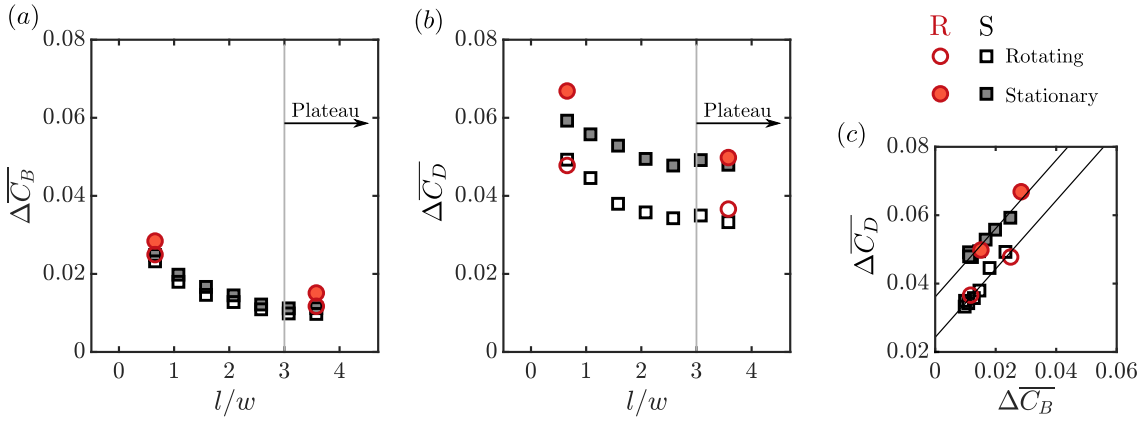

Figure 16: Evolution of (a) the base drag $\Delta\overline{C_B} = \overline{C_B} - \overline{C_{B0}}$ and (b) total drag $\Delta\overline{C_D} = \overline{C_D} - \overline{C_{D0}}$ of the body as a function of the wheel-to-base distance l/w. Different wheel shapes (sharp-edged-shoulder wheels (S, colored in black) or rounded-shoulder wheels (R, colored in red)) and different wheel states (rotating or stationary) are considered. The relationship between $\Delta\overline{C_D}$ and $\Delta\overline{C_B}$ is shown in (c).

in Pavia & Passmore (2017). Further investigation of the velocity measurements not shown here for brevity confirms that the salient features of wheel-vehicle interactions derived from the rotating cases can be gained in the same way by using the stationary cases. The main aspects of wheel-vehicle interactions for this square-back body, namely the global forcing of the vehicle wake and the local near-wake interactions, are therefore not related to the wheel state.

Appendix B. Evaluating the effect of mass exchange on the base drag

In Bao *et al.* (2022), a physical model based on a momentum balance of the wake was proposed to link the mass exchange observed in their study and the concomitant base drag changes. This model was derived from fundamental studies focusing on the effect of base suction on the base pressure of either a 2-D D-shaped cylinder (Bearman, 1967) or a 3-D bluff body (Hsu *et al.*, 2021). In these two reference works, a simple relation between the base drag change $\Delta\overline{C_B}$ and the suction flow rate q:

$$\Delta\overline{C_B} = \frac{2q}{HWU_0} = 2C_q, \tag{9}$$

was found to hold for small suction flow rate coefficient C_q ($C_q < 0.03$ in Hsu *et al.* (2021)). In such situations, fluid particles continuously enter the mean recirculating region and therefore loose their longitudinal momentum. By writing that a pressure decrease at the base is responsible for this momentum flux balance, one gets $\Delta F_x = (\rho q)U_0$. Normalizing the corresponding quantities, the simple relation $\Delta\overline{C_B} = 2C_q$ is then obtained. This model was then found in Bao *et al.* (2022) to be able to explain the results, such as the scalings for the base drag. Considering the overall accordance of the present wheel situation with the obstacle situation, this model is now used to give a global point-of-view linking the base drag variation and the local mass exchange observed in the present study.

We start from the base drag evolution shown in figure 13. A gradual increase of $\Delta\overline{C_B}^*$ of ~ 0.014 from $l/w = 3.09$ to $l/w = 0.65$ is measured for all configurations. Accompanied by this, pressure measurements show a continuous decrease of pressure and increase of periodic dynamics at the bottom trailing edge of the vehicle with decreasing l/w at $l/w < 3$. Also, the mean properties in the rear wheel wake are measured to be preserved for different l/w cases. As depicted in the sketches in figure 17, we therefore assume a rectangular region with a length of $3w$ downstream of the rear wheels having the ability to induce mass exchange from the vehicle wake. With decreasing l/w, the area of the mass exchange surface $S_e = (3w - l)w$ increases linearly at $l/w < 3$. A space-averaged mass transfer velocity U_e can be defined by $q = 2S_eU_e$ (2 is here the number of rear wheels). Using relation 9, U_e/U_0 can be easily estimated with $U_e/U_0 = HW\Delta\overline{C_B}^*/(4S_e)$ for all the cases in the

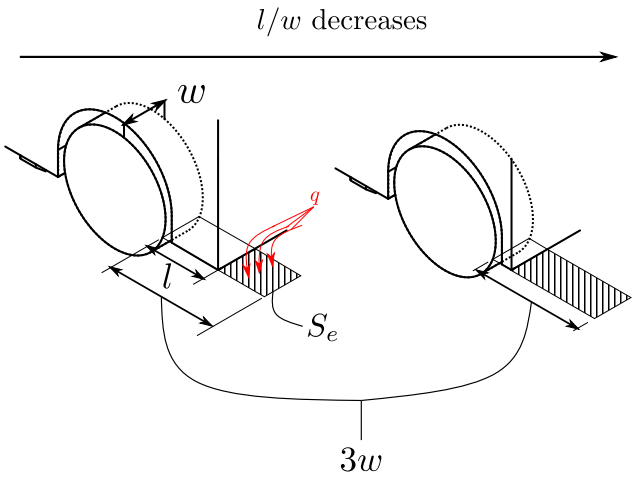

Figure 17: Schematics of the surface of mass exchange in the drag-sensitive regime $l/w < 3$.

drag-sensitive regime ($l/w < 3$). For the cases with the shortest vehicle ($l/w = 0.65$), U_e/U_0 is found to be ~ 0.055, which is a good order of magnitude of the downward vertical velocities measured in figure 10(c) and 14(c, d) near $z/H = G/H$. The present experimental data is therefore in good agreement with the physical model proposed in Bao *et al.* (2022).

References

Aultman, M., Auza-Gutierrez, R., Disotell, K. & Duan, L. 2022 Effects of wheel rotation on long-period wake dynamics of the drivaer fastback model. *Fluids* **7** (1), 19.

Bao, D., Borée, J., Haffner, Y. & Sicot, C. 2022 Near wake interactions and drag increase regimes for a square-back bluff body. *J. Fluid Mech.* **936**, A2.

Barros, D., Borée, J., Cadot, O., Spohn, A. & Noack, B.R. 2017 Forcing symmetry exchanges and flow reversals in turbulent wakes. *J. Fluid Mech.* **829**, R1.

Bearman, P.W. 1967 The effect of base bleed on the flow behind a two-dimensional model with a blunt trailing edge. *Aeronaut. Q.* **18** (3), 207–224.

Bonnavion, G. & Cadot, O. 2018 Unstable wake dynamics of rectangular flat-backed bluff bodies with inclination and ground proximity. *J. Fluid Mech.* **854**, 196–232.

Bradshaw, P. 1973 Effects of streamline curvature on turbulent flow. *Tech. Rep.*. Advisory Group for Aerospace Research and Development Paris (France).

Brandt, A., Berg, H., Bolzon, M. & Josefsson, L. 2019 The effects of wheel design on the aerodynamic drag of passenger vehicles. *Tech. Rep.* 2019-01-0662. Society of Automotive Engineers, Inc.

Cogotti, A. 1983 Aerodynamic characteristics of car wheel. *Int. J. of Vehicle Design* **SP3**.

Croner, E., Bézard, H., Sicot, C. & Mothay, G. 2013 Aerodynamic characterization of the wake of an isolated rolling wheel. *Int. J. Heat Fluid Flow* **43**, 233–243.

Elofsson, P. & Bannister, M. 2002 Drag reduction mechanisms due to moving ground and wheel rotation in passenger cars. *Tech. Rep.* 2002-01-0531. Society of Automotive Engineers, Inc.

Grandemange, M., Gohlke, M. & Cadot, O. 2013 Turbulent wake past a three-dimensional blunt body. part 1. global modes and bi-stability. *J. Fluid Mech.* **722**, 51.

Haffner, Y., Borée, J., Spohn, A. & Castelain, T. 2020 Mechanics of bluff body drag reduction during transient near-wake reversals. *J. Fluid Mech.* **894**, A14.

Haffner, Y., Castelain, T., Borée, J. & Spohn, A. 2021 Manipulation of three-dimensional asymmetries of a turbulent wake for drag reduction. *J. Fluid Mech.* **912**, A6.

Haffner, Y., Li, R., Meldi, M. & Borée, J. 2022 Drag reduction of a square-back bluff body under constant cross-wind conditions using asymmetric shear layer forcing. *Int. J. Heat Fluid Flow* **96**, 109003.

Heft, A. I., Indinger, T. & Adams, N. A. 2012 Introduction of a new realistic generic car model for aerodynamic investigations. *Tech. Rep.* 2012-01-0168. Society of Automotive Engineers, Inc.

Hobeika, T. & Sebben, S. 2018 Tyre pattern features and their effects on passenger vehicle drag. *Tech. Rep.* 2018-01-0710. Society of Automotive Engineers, Inc.

Hobeika, T., Sebben, S. & Landstrom, C. 2013 Investigation of the influence of tyre geometry on the aerodynamics of passenger cars. *Tech. Rep.* 2013-01-0955. Society of Automotive Engineers, Inc.

Hsu, E.C., Pastur, L., Cadot, O. & Parezanović, V. 2021 A fundamental link between steady asymmetry and separation length in the wake of a 3-d square-back body. *Exp. Fluids* **62** (5).

Huminic, A. & Huminic, G. 2017 Aerodynamic study of a generic car model with wheels and underbody diffuser. *Int. J. Automot. Technol.* **18** (3), 397–404.

Josefsson, E., Hobeika, T. & Sebben, S. 2022*a* Evaluation of wind tunnel interference on numerical prediction of wheel aerodynamics. *J. Wind Eng. Ind. Aerodyn.* **224**, 104945.

Josefsson, E., Hobeika, T., Sebben, S. & Urquhart, M. 2022*b* Investigation of tyre pattern effect on the aerodynamics of a passenger vehicle. *J. Fluids Eng.* **144** (11), 111209.

Krajnović, S. & Davidson, L. 2005 Influence of floor motions in wind tunnels on the aerodynamics of road vehicles. *J. Wind Eng. Ind. Aerodyn.* **93** (9), 677–696.

Krajnović, S., Sarmast, S. & Basara, B. 2011 Numerical investigation of the flow around a simplified wheel in a wheelhouse. *J. Fluids Eng.* **133** (11).

Landström, C., Löfdahl, L. & Walker, T. 2009 Detailed flow studies in close proximity of rotating wheels on a passenger car. *Tech. Rep.* 2009-01-0778. Society of Automotive Engineers, Inc.

Landström, C., Walker, T., Christoffersen, L. & Löfdahl, L. 2011 Influences of different front and rear wheel designs on aerodynamic drag of a sedan type passenger car. *Tech. Rep.* 2011-01-0165. Society of Automotive Engineers, Inc.

Le Good, G.M., Howell, J.P., Passmore, M.A. & Cogotti, A. 1998 A comparison of on-road aerodynamic drag measurements with wind tunnel data from pininfarina and mira. *Tech. Rep.* 980394. Society of Automotive Engineers, Inc.

Legeai, A. & Cadot, O. 2020 On the recirculating flow of three-dimensional asymmetric bluff bodies. *Exp. Fluids* **61** (12), 1–6.

Lorite-Díez, M., Jiménez-González, J.I., Pastur, L., Martínez-Bazán, C. & Cadot, O. 2020 Experimental analysis of the effect of local base blowing on three-dimensional wake modes. *J. Fluid Mech.* **883**.

Mercker, E. & Knape, H.W. 1989 Ground simulation with moving belt and tangential blowing for full-scale automotive testing in a wind tunnel. *Tech. Rep.* 890367. Society of Automotive Engineers, Inc.

Mlinaric, P. & Sebben, S. 2008 Investigation of the influence of tyre deflection and tyre contact patch on cfd predictions of aerodynamic forces on a passenger car. In *7th MIRA International Vehicle Aerodynamics Conference*.

Patel, D., Garmory, A. & Passmore, M. 2022 On the wake of an isolated rotating wheel: An experimental and numerical investigation. *J. Wind Eng. Ind. Aerodyn.* **227**, 105049.

Pavia, G. 2019 Characterisation of the unsteady wake of a square-back road vehicle. PhD thesis, Loughborough University.

Pavia, G. & Passmore, M. 2017 Characterisation of wake bi-stability for a square-back geometry with rotating wheels. In *FKFS Conference*, pp. 93–109. Springer.

Pavia, G., Passmore, M.A., Varney, M. & Hodgson, G. 2020 Salient three-dimensional features of the turbulent wake of a simplified square-back vehicle. *J. Fluid Mech.* **888**, A33.

Perry, A. K. & Passmore, M. 2013 The impact of underbody roughness on rear wake structure of a squareback vehicle. *Tech. Rep.* 2013-01-0463. Society of Automotive Engineers, Inc.

Regert, T. & Lajos, T. 2007 Description of flow field in the wheelhouses of cars. *Int. J. Heat Fluid Flow* **28** (4), 616–629.

Reiss, J., Haag, L. & Indinger, T. 2019 Cfd investigation on fully detailed and deformed car tires. *Int. J. Automot. Eng.* **10** (4), 324–331.

Rejniak, A. A. & Gatto, A. 2021 Influence of rotating wheels and moving ground use on the unsteady wake of a small-scale road vehicle. *Flow Turbul. Combust.* **106** (1), 109–137.

Schuetz, T. 2016 *Aerodynamics of road vehicles*. Society of Automotive Engineers, Inc.

Strachan, R.K., Knowles, K. & Lawson, N.J. 2007 The vortex structure behind an ahmed reference model in the presence of a moving ground plane. *Exp. Fluids* **42** (5), 659–669.

Varney, M. 2020 Base drag reduction for squareback road vehicles. PhD thesis, Loughborough University.

Varney, M., Passmore, M., Swakeen, R. & Gaylard, A. 2020 Parametric study of reduced span side tapering on a simplified model with wheels. *Tech. Rep.* 2020-01-0680. Society of Automotive Engineers, Inc.

Wang, S., Avadiar, T., Thompson, M. C. & Burton, D. 2019 Effect of moving ground on the aerodynamics of a generic automotive model: The drivaer-estate. *J. Wind Eng. Ind. Aerodyn.* **195**, 104000.

Wang, Y. 2019 Experimental study of wheel-vehicle aerodynamic interactions. PhD thesis, Chasseneuil-du-Poitou, Ecole Nationale Supérieure de Mécanique et d'Aérotechnique.

Wang, Y., Sicot, C., Borée, J. & Grandemange, M. 2020 Experimental study of wheel-vehicle aerodynamic interactions. *J. Wind Eng. Ind. Aerodyn.* **198**, 104062.

Wäschle, A. 2007 The influence of rotating wheels on vehicle aerodynamics-numerical and experimental investigations. *Tech. Rep.* 2007-01-0107. Society of Automotive Engineers, Inc.

Wickern, G., Zwicker, K. & Pfadenhauer, M. 1997 Rotating wheels-their impact on wind tunnel test techniques and on vehicle drag results. *Tech. Rep.* 970133. Society of Automotive Engineers, Inc.

Wittmeier, F., Kuthada, T., Widdecke, N. & Wiedemann, J. 2014 Model scale based process for the development of aerodynamic tire characteristics. *Tech. Rep.* 2014-01-0585. Society of Automotive Engineers, Inc.

718 Wittmeier, F., Widdecke, N., Wiedemann, J., Lindener, N. & Armbruster, R.
719 2013 Reifenentwicklung unter aerodynamischen aspekten. *ATZ-Automobiltechnische Zeitschrift*
720 **115** (2), 144–150.

721 Yu, X., Jia, Q., Rashidi, M. M. & Yang, Z. 2020 Comprehensive investigating on the aerody-
722 namic influences of the wheel contact patch. *J. Appl. Comput. Mech.* **6** (4), 934–955.

723 Yu, X., Jia, Q. & Yang, Z. 2022 Comprehensive study of the aerodynamic influence of ground
724 and wheel states on the notchback drivaer. *Energies* **15** (3), 1124.